A Biomimetic Miniaturized *In Vitro* Model to Target Early Markers of Neonatal Pulmonary Vascular Injury

Motaharehsadat Heydarian[1,2*], Ali Doryab[1,2], Juan Henao[3], Benjamin Schubert[3], Otmar Schmid[1], Anne Hilgendorff [1,4,5*]

[1]Institute for Lung Health and Immunity and Comprehensive Pneumology Center, Helmholtz Zentrum München, Munich, Germany, Member of the German Lung Research Center (DZL)

[2]Department of Medicine, University of Cambridge, CB2 0QQ,UK Cambridge, United Kingdom

[3]Institute for Computational Biology, Helmholtz Zentrum München, Member of the German Lung Research Center (DZL), Munich, Germany

[4]Dr. von Hauner Children's Hospital, University Hospital Ludwig-Maximilian University, Munich, Germany

[5]School of Medicine and Health Sciences, Department of Paediatrics, Section of Neonatology, Pediatric Intensive Care, Pediatric Cardiology, Pediatric Pneumology and Allergology, and Research Centre Neurosensory Science, Carl von Ossietzky University Oldenburg, Germany

[*]Corresponding authors:

Prof. Dr. Anne Hilgendorff
University Clinic for Paediatrics and Adolescent Medicine
(Elisabeth Children's Hospital)
Oldenburg Hospital AöR
Rahel-Straus-Str. 10
26133 Oldenburg
Carl von Ossietzky University, European Medical
Medical School, Oldenburg
Email: anne.hilgendorff@uni-oldenburg.de

Dr. Motaharehsadat Heydarian
Department of Medicine, University of Cambrisge,
Addenbrookes Hospital, Hills Rd, Cambridge CB2 0QQ
Email: mh2348@cam.ac.uk

Abstract

Pulmonary vascular disease (PVD) is a major contributor to morbidity in preterm infants as it is associated with a significant risk to devevlop pulmonary hypertension, especially in infants diagnosed with prematurity-associated lung disease (PLD), also known as bronchopulmonary dysplasia (BPD). However, the earliest events of vascular injury triggered by postnatal mechanical and oxygen-related stress remain poorly understood, largely due to the limitations of existing *in vitro* models. We therefore developed a biomimetic, miniaturized Pulmonary *In Vitro* Perfusion (PIPE) system that integrates pathophysiologically relevant shear stress with controlled oxygen exposure for the exposure of a human co-culture of pulmonary microvascular endothelial cells and pulmonary artery smooth muscle cells. Advancing the system to a triple co-culture, circulating THP-1 monocytes capture early endothelial-smooth muscle-immune cell interactions.

Shear stress alone induced early proliferative and extracellular matrix-related responses in endothelial cells and resulted in enhanced monocyte recruitment without disrupting barrier integrity. When combined with oxygen exposure, the model revealed a dose-dependent injury pattern: moderate hyperoxia (FiO_2 0.40) had minimal acute effects, whereas severe hyperoxia (FiO_2 0.85) impaired endothelial barrier function, increased ROS production, promoted monocyte transmigration, activated apoptosis (Caspase 3), and elevated soluble collagen synthesis. This dynamic *in vitro* system reveals early drivers in vascular injury and recapitulates key characteristics of PVD, thereby introducing a translational platform for the dissection of disease mechanisms and evaluation of therapeutic strategies targeting vascular injury in the developing lung.

Keywords:

Pulmonary vascular disease; PVD; Vascular injury; Preterm-associated lung disease; Bronchopulmonary dysplasia; Biomimetic *in vitro* perfusion model; Shear stress; Hyperoxia

Introduction

Preterm birth, affecting nearly 10% of all live births, renders the immature lung highly susceptible to postnatal injury. Life-saving interventions such as mechanical ventilation and oxygen therapy (1, 2), together with pre- or postnatal infection, are known to disrupt alveolar and vascular development (3, 4). The subsequent development of prematurity-associated lung disease (5) or bronchopulmonary dysplasia (BPD), is inextricably linked to lifelong impairment, including a substantial risk for the development of pulmonary hypertension (PH) (6, 7). A key but often under-recognized component of BPD pathophysiology is pulmonary vascular disease (PVD). Here, the immature, structurally limited vascular bed is abruptly exposed to full systemic blood flow, hemodynamic stressors (e.g., patent ductus arteriosus, parenteral fluids), fluctuating oxygen levels, and mechanical forces introduced by artificial ventilation(8–10). Together, these stressors trigger endothelial injury, inflammation, and remodeling, including excessive extracellular matrix (ECM) deposition and smooth muscle thickening (11). PVD affects all infants with BPD to a varying degree, often escapes clinical monitoring, but results in an up to 30% risk for the development of PH in infants with moderate and severe BPD (12).

Despite its clinical relevance, the earliest and potentially preventable events underlying postnatal vascular injury remain poorly understood. On the one hand, existing models rarely capture the early events of pathologic endothelial-smooth muscle interactions. On the other hand, most models rely on maximized oxygen concentrations while overlooking the double-hit injury provoked by shear stress in the presence of clinically relevant, moderate hyperoxia (13–15). This creates a critical gap in understanding how postnatal mechanical and oxygen-related cues jointly shape early PVD.

We therefore developed a miniaturized Pulmonary *In Vitro* Perfusion (PIPE) system that applies controlled, perfusion-generated disease-relevant shear stress to human primary microvascular endothelial cells (hPMECs) and pulmonary artery smooth muscle cells (hPASMCs) at levels relevant to the microvasculature of the developing lung, while enabling precise manipulation of oxygen exposure- features not attainable in conventional culture systems. The applied wall shear stress levels were derived from clinical data and previously published models (16, 17).

We then recreated innate immune-vascular interactions under dynamic flow in a triple co-culture model by circulating monocytic THP-1 cells, known to play a critical role in neonatal lung inflammation and PVD (18–20). Exposure of the triple coculture to room air (FiO_2=0.21), clinically prevalent moderate hyperoxia (FiO_2=0.40), or severe hyperoxia (FiO_2=0.85) under dynamic flow conditions in comparison to static flow allowed us to identify critical events of early microvascular injury. We successfully demonstrate that shear stress alone induces early proliferative and ECM-related responses in vascular cells and enhances monocyte recruitment. In this context, hyperoxia acted in a dose-dependent manner: moderate concentrations had limited acute effects, whereas severe hyperoxia triggered impaired barrier integrity, increased ROS production, heightened monocyte transmigration, apoptosis, and early collagen synthesis. Key observations were validated in a preclinical mouse model following neonatal hyperoxia exposure into adolescence.

Taken together, these data identify the earliest events of vascular injury, including immune alterations during postnatal injury, and establish the PIPE platform as a biomimetic, translationally relevant system for dissecting the mechanisms underlying BPD-associated PVD.

Results

Postnatally, the functionally and structurally immature microvasculature that characterizes the developing lung in preterm neonates is exposed to elevated mechanical forces, i.e., shear stress introduced by systemic stroke volumes and artificial ventilation (8). To investigate the earliest and previously uncharacterized effects of shear stress and hyperoxia on the lung microvasculature, we engineered and validated a multi-well, miniaturized biomimetic PIPE system. The platform incorporates a basal endothelial layer (hPMECs) co-cultured with apical human pulmonary arterial smooth muscle cells (hPASMCs) and enables the controlled exposure to defined levels of shear stress (Fig. 1A-B). In the next step, we advanced this system to allow the simultaneous regulation of perfusion and oxygen, thereby mimicking a clinically relevant postnatal treatment regimen (9, 21).

Successful implementation of a biomimetic platform to investigate early pathophysiologic cues in microvascular injury

Computational flow simulations of the main chamber revealed a stable and spatially uniform velocity field across the channel (Fig. 1Cii), confirming that applying perfusion to the basal compartment produced consistent flow conditions along the endothelial monolayer. The velocity profile across the channel height (Y-axis) demonstrated a symmetric parabolic distribution, characteristic of laminar flow, further supporting uniform shear delivery within the endothelial region. Correspondingly, wall shear stress (WSS) levels at the endothelial surface reached ~10.9 dyn/cm^2 under a perfusion rate of 2 mL/min (Fig. 1Ciii). This level is consistent with data obtained in pediatric PH patients (16) and consistent with previously published models for human pulmonary endothelial cells (17).

To validate effective transmission of shear stress to adherent endothelial cells in the PIPE system, we cultured EA.hy926 cells on the basal surface of the Transwell membrane and exposed them to 24 h of controlled shear (10.9 dyn/cm^2). Endothelial cells exhibited marked alignment of the F-actin cytoskeleton in the direction of flow (Fig. 1D). Importantly, no evidence of cytotoxicity or compromised monolayer integrity was observed at this shear magnitude.

Succesfully establishing a physiologically relevant human-based co-culture model within the PIPE system, we cultured primary human pulmonary microvascular endothelial cells (hPMECs) and human pulmonary arterial smooth muscle cells (hPASMCs) on the basal and apical surfaces of ECM coated-Transwell inserts, respectively (Fig. 1E). Confocal imaging confirmed the formation of a confluent endothelial monolayer characterized by continuous VE-cadherin junctions and organized F-actin architecture, while hPASMCs formed a robust monolayer on the apical surface (Fig. 1F). Functional assessment of barrier integrity demonstrated a progressive decline in apparent permeability (P_{app}), decreasing from 8.4×10^{-6} cm/s on day 1 to 2.6×10^{-6} cm/s by day 5 ($p < 0.0001$), consistent with formation of the endothelial barrier (Fig. 1G). Importantly, permeability remained stable thereafter, with no significant difference between day 5 and day 6 ($p = 0.884$), indicating that the co-culture model maintains barrier integrity under extended culture conditions.

Shear stress provokes early vascular injury and remodeling in a model of PVD, together with enhanced monocyte recruitment

Exposure of the hPMEC/hPASMC co-culture model to a shear stress of 10.9 dyn/cm^2 for 8 h induced several notable biological responses compared with static culture conditions (Fig. 2). Shear stress significantly increased endothelial cell proliferation, as reflected by a higher proportion of Ki67$^+$ cells on the basal hPMEC layer (Fig. 2A-B). In contrast, endothelial barrier function remained unchanged, with no significant differences in apparent permeability (P_{app}) between static and dynamic conditions (Fig. 2E; 8.5 x 10^{-7} vs. 1.1 x 10^{-6}, mean ± SD, p-value= 0.054). However, shear stress elicited a marked increase in nitrite secretion (Fig. 2C; 15.3 vs. 23.4, mean ± SD, p-value = 0.004) and elevated total soluble collagen production in endothelial and smooth muscle cells (Fig. 2D; 3.9 vs.7.6, mean ± SD, p-value = 0.014), suggesting early extracellular matrix (ECM) remodeling.

To further dissect cell-type–specific mechanobiological responses, we performed MACE RNA-sequencing on isolated hPASMCs and hPMECs following shear exposure (Fig. 2F). Endothelial cells exhibited robust transcriptional activation, dominated by the upregulation of cytokine- and ECM-associated genes, consistent with the observed increases in nitrite and soluble collagen. Downregulated transcripts included key regulatory mediators such as HSP90, CAVIN2, and CYP1A1, indicating involvement of eNOS- and cytochrome p450 signaling pathways. In parallel, hPASMCs displayed pronounced induction of inflammatory and matrix-related genes, including TGFB1, IL1B, and COL6A, alongside the repression of developmental regulators such as TBX1. Pathway enrichment using the Reactome database confirmed activation of cytokine signaling pathways (IL-4/IL-13 signaling) and ECM remodeling processes (collagen formation) in hPMECs, with hPASMCs exhibiting a highly overlapping profile characterized by upregulated collagen biosynthesis, integrin-mediated interactions, and fibrillar matrix organization (Fig. 2F).

When establishing a dynamic triple co-culture by the successful introduction of circulating THP-1 monocytes alongside the endothelial layer (Fig. 2G), we were able to demonstrate that shear stress markedly enhanced THP-1 transmigration across the hPMEC barrier toward the hPASMC layer, as visualized by confocal imaging (Fig. 2H). The finding was confirmed by quantitative analysis (Fig. 2I), indicating increased monocyte recruitment

and transmigration under conditions of shear stress, further contributing to the pattern of matrix remodelling and endothelial injury outlined above.

Severe but not moderate hyperoxia enhances vascular injury and remodeling in the context of shear stress in a triple co-culture model of PVD

Building on the established dynamic triple co-culture model, we next sought to mimic postnatal exposure to clinically relevant oxygen levels by subjecting the system to normoxia (FiO_2 = 0.21), moderate (FiO_2 = 0.40) or severe hyperoxia (FiO_2 = 0.85) for 8 h in the presence of shear stress (Fig. 3A). In this double-hit model, exposure to moderate hyperoxia, reflecting oxygen levels commonly used in neonatal care, did not significantly alter endothelial barrier integrity (Fig. 3B), ROS generation (Fig. 3C), monocyte transmigration (Fig. 3D, E), caspase-3 activity (Fig. 3F, G), collagen IV deposition (Fig. 3H), or total soluble collagen levels (Fig. 3I), when compared with normoxia conditions in the triple co-culture model. In contrast, severe hyperoxia (FiO_2 = 0.85) resulted in reduced barrier integrity and markedly increased ROS production (Fig. 3B–C), accompanied by enhanced THP-1 monocyte transmigration across the endothelial layer (Fig. 3D, E) when compared to normoxia. Severe hyperoxia also triggered a significant rise in caspase-3 expression (Fig. 3F, G), indicating increased apoptotic activity, as well as elevated levels of total soluble collagen (Fig. 3I), suggestive of extracellular matrix remodeling.

Collagen IV expression remained unchanged across all oxygen conditions (Fig. 3H).

In a preclinical model, we exposed neonatal mice at postnatal day 5-7, i.e. in the saccular stage of lung development (E17.5–P5; equivalent to human gestational age 27–36 weeks) to moderate (FiO_2=0.40) or severe hyperoxia (FiO_2=0.85) for 8h (21, 22). Severe hyperoxia led to enhanced monocyte/macrophage recruitment, induction of apoptosis, and collagen deposition in the alveolar area, together with a reduction in the number of small blood vessels (20–100 μm) 3 weeks after exposure **(Fig. 4A-E).** In contrast to severe hyperoxia, moderate oxygen supplementation induced only milder changes to monocyte recruitment, apoptosis, and collagen deposition, resulting in no significant changes to microvessel number. While the animal experiments were performed to relate the effects observed *in vitro* to early changes following hyperoxia exposure *in vivo* and early signs of neonatal pulmonary injury including effects on pulmonary microvessel

density, macrophage infiltration, apoptosis and collagen deposition reflect the pathologic hallmarks observed *in vitro*, the *in vivo* setting was not designed to exactly mirror the conditions applied in the *in vitro* PIPE setting.

Discussion

Here is the discussion, I wanted to include some new parts in it as instructed “The severe impairment of vascular development is a central component of prematurity-associated lung disease (PLD) and is caused by multiple postnatal insults impacting the immature pulmonary vascular bed, ultimately promoting PVD (5). The rise in vascular resistance due to microvessel rarefaction and progressive remodeling parallels clinical evidence of increased right ventricular afterload in infants with BPD (23, 24). Despite the clinical importance of PVD and its severe risk to progress into PH(25), the early drivers and pathophysiologic cues remain insufficiently understood, hindering the development of effective preventive or therapeutic strategies. We therefore developed an *in vitro* model designed to recapitulate key postnatal conditions, namely hemodynamic stimulation and hyperoxia, that the immature, rarefied vascular bed of the preterm lung is exposed to early after birth.

We established a human-based coculture of hPMEC/hPASMC with robust and comparable barrier integrity (26) on a porous membrane integrated into a millifluidic PIPE system that circulates medium across the basal (endothelial) compartment to generate quasi-continuous, unidirectional flow and thereby shear stress (Fig. 1). In the study presented, static culture conditions were used as a comparator to widely used conventional cell culture models operating without flow, rather than a physiological baseline as the absence of flow does not reflect the native mechanical environment in the the lung microvasculature. Future studies can, however, incorporate defined physiological and pathological hemodynamic regimes, such as variations in shear stress magnitude to better model disease-relevant transitions and enhance the translational relevance of the platform.

Based on previous characterizations of wall shear stress in pediatric patients with pulmonary arterial hypertension, wall shear stress in distal small pulmonary arteries (diameters 50-500 µm) ranged from 6.3 to 15.8 dyn/cm^2, depending on disease severity

(16). Accordingly, we selected a wall shear stress of approximately 10.9 dyn/cm^2 at a perfusion rate of 2 mL/min, a value consistent with previously published models for human pulmonary endothelial cells (17).

Leveraging the PIPE system, we identified early (8 h) shear stress-induced responses in endothelial cells consistent with initial features of PVD in PLD. We detected increases in the proliferation marker Ki67, nitrite release, and soluble collagen without evidence of overt cytotoxicity or barrier disruption compared with static (no-flow) conditions (Fig. 2A-E). Complementing these findings, transcriptomic profiling of the co-culture demonstrated strong regulation of pathways associated with ECM deposition and intercellular crosstalk (Fig. 2F). The regulation of *HSP90*, *CAVIN2,* and *CYP1A1* indicated a cellular stress response related to (*TGFB1*-dependent) transdifferentiation in hPMECs as previously described (27–30). In line with these findings, Reactome database analysis highlighted the regulation of inflammation and matrix formation in hPSMCs, indicated by the upregulation of *TGFB1*, *ILB1,* and *COL6A* transcription and accompanied by the downregulation of *TBX1*, known for its critical functions in vascular development (31). The identified mechanisms that characterize early injury hold potential for the development of therapeutic strategies (32, 33).

Expanding the system to a triple coculture of hPMECs, hPASMCs, and circulating THP-1 monocytes enabled modeling of early innate immune-vascular interactions reflective of the inflammatory milieu characterizing neonatal lung disease (19). By the use of our biomimetic platform, we demonstrate that shear stress promoted monocyte recruitment and transmigration across the endothelial layer toward the hPASMC compartment, recapitulating early inflammatory infiltration (Fig. 2G-I).

Despite extensive evidence that hyperoxia contributes to lung vascular pathology (34), the combined influence of clinically relevant oxygen ranges and shear stress has remained incompletely characterized. To address the impact of clinically prevalent treatments in a double hit model, we examined the combined effects of shear stress and graded hyperoxia (35, 36) (Fig. 3). Even brief exposure to severe hyperoxia (FiO_2 = 0.85) markedly impaired EC-SMC function in a dose-dependent manner (Fig. 3B- I), consistent with clinical and preclinical observations in neonates and mice (22, 37). Severe hyperoxia increased ROS generation, enhanced THP-1 transmigration, activated caspase-3-

dependent apoptosis, and elevated total soluble collagen production. Notably, collagen IV remained unchanged across conditions, indicating that basement membrane remodeling had not yet occurred within this acute (8h) exposure window (Fig. 3H). Although moderate hyperoxia has been shown to induce ECM remodeling in human fetal airway SMCs (38), our observations reveal a more pronounced early response in the pulmonary vascular compartment with an increase in total soluble collagen without parallel changes in collagen IV, likely reflecting rapid initiation of ECM synthesis before deposition of more structured basement membrane-associated collagens.

In contrast to the dramatic changes induced by severe hyperoxia, moderate hyperoxia did not provoke changes in the outlined indicators of endothelial cell injury. Highlighting this important difference in the effect of oxygen concentrations on the vascular wall, future studies should address the clinically relevant aim to more adequately target the delicate balance between the beneficial (vasodilatory) (34, 39) and detrimental effects of oxygen supplementation with the potential to either mitigate or amplify shear stress–induced injury [60]. However, the absence of active CO_2 control during oxygen exposure experiments and the use of atmospheric FiO_2 (0.21) as a reference condition may not fully recapitulate physiologic conditions, as standard culture systems can provoke relative hyperoxia due to dissolved oxygen tensions as compared to the pulmonary microenvironment.

In summary, our study presents a platform that allows the description of critical early effects of clinically prevalent conditions on the vascular wall. Our study detailed the detrimental effects of increased shear stress, including the identification of candidate pathways that can inform future therapeutic approaches in BPD-associated PVD. The platform enabled the delineation of added injury mechanisms, such as hyperoxia under biologically relevant flow conditions, while incorporating the important role of the immune system, demonstrating their interaction with the vascular wall. Compared to conventional *in vitro* cultures that are based on static, mostly monocultural or selected co-culture models, the PIPE platform enables the combination of controlled flow conditions with multicellular co-cultures, including the circulation of immune cells. The model that can be scaled to multiple-hit conditions allow the interrogation of cell-cell interaction dynamics under the impact of defined mechanical and biochemical stressors (40–43). While the

PIPE platform does not recapitulate mechanical ventilation in the sense of alveolar stretch, it is important to note that shear stress *in vivo* is impacted by mechanical ventilation, especially in the preterm infant where the significant levels of positive end-expiratory pressure (PEEP) as well as inhomogeneous ventilation with a side-by-side of overinflation and atelectasis recurrently add to changes in pressure and blood in the developing lung, provoking strain. The alteration of intrathoracic pressure and ventilation-dependant changes in pulmonary vascular resistance and blood flow distribution contribute to endothelial activation and vascular remodelling (44). As such, PIPE provides a biomimetic platform that may enhance *in vitro* to *in vivo* translation (45). Supporting the translational relevance, we confirmed the immune-driven characteristics of lung injury in a preclinical BPD mouse model and the persistence of these changes beyond alveolarization (10, 46).

Taken together, our PIPE model – integrating mechanical forces into a double-hit model when adding oxidative stress while allowing to study immune cell interactions – offers a controlled and reductionist *in vitro* system that captures key aspects of the pulmonary microvascular responses to injury and surpasses static or single-parameter culture models in translational relevance. While the PIPE platform mirrors hallmarks of early endothelial injury provoked by shear stress and hyperoxia in the neonatal mouse lung, it does not fully capture the *in vivo* complexity of the gas-exchange region, including the multi-layered alveolar architecture and epithelial-endothelial interactions. Incorporating additional cellular layers will be important to better recapitulate the alveolar interface and to study interaction mechanisms relevant to the developing lung. Further integration of *in vivo*-like features or advanced imaging approaches will be required to validate and extend these findings. Future work will also benefit from extending exposure duration, optimizing co-culture media (47), validating cell-type–specific transcriptomes under migratory conditions, and incorporating additional neonatal-relevant therapeutic interventions such as retinoic acid or nitric oxide (48, 49).

Materials and Methods

Design and fabrication of the Pulmonary *In Vitro* Perfusion (PIPE) system

This study utilized an in-house multi-well Pulmonary In *Vitro* Perfusion (PIPE) millifluidic system. The setup consists of five independent miniaturized bioreactors that run in parallel and are connected to a central chamber and reservoir. The main chamber is divided into basal and apical compartments by a polycarbonate membrane. In the main chamber, an interface (outlet) connects the apical compartment to the air-tight container to control temperature, humidity, and oxygen concentration. The culture medium in the basal compartment was circulated to simulate blood flow with a peristaltic pump (Shenzhen LabVI-II). Once the cell cultures were established, they were transferred to the PIPE system and subjected to quasi-continuous, unidirectional flow generating shear stress. Static culture conditions were used as a comparator to widely used conventional cell culture models operating without flow. For oxygen exposure experiments, the PIPE setup was placed in an airtight container connected to an oxygen concentrator, generating oxygen concentrations with a fraction of inspired oxygen (FiO_2) of 0.21, 0.40, and 0.85, respectively. Oxygen concentrations were monitored using an oxygen meter (Greisinger Instruments; oxygen sensor GOEL 381; **Fig. 1B**).

Computational shear stress simulation

Wall shear stress (WSS) on endothelial cells cultured on the basal side of a Transwell insert was simulated using COMSOL Multiphysics (version 6.3). A 2D rectangular domain (6.5 mm × 0.4 mm) representing the flow channel beneath the cell layer was modelled with steady-state, incompressible, laminar Navier-Stokes equations. The culture medium was treated as a Newtonian fluid (density 1000 kg/m^3, viscosity (μ) 0.93 mPa·s (50)). A uniform inlet velocity corresponding to a perfusion rate of 2 mL/min (Q) was applied, with zero pressure at the outlet and no-slip conditions at the top (cell surface) and bottom walls.

The domain was meshed with boundary layer refinement at the cell layer, and a stationary solver was used to compute velocity and shear stress. WSS on the endothelial monolayer was calculated (Equation 1) from the viscous stress tensor, and average WSS was obtained via line integration along the cell-covered boundary;

$$WSS = \frac{6\mu Q}{wh^2} \text{ (Eq.1)}$$

Primary human cell sources and cell lines

Primary human pulmonary microvascular endothelial cells (hPMEC) (Promo Cell, #C-12282) were cultured in endothelial cell growth medium MV (Promo Cell, #C-22020). Primary human pulmonary artery smooth muscle cells (hPASMC) (ThermoFisher, #C0095C) were cultured in SmGMTM-2 smooth muscle cell growth medium -2 BulletKitTM (Lonza, CC-3182). Human monocytic cell line (THP1) (BIOZOL, #ADD-C0003024) was cultured in RPMI-1640 (Gibco/Thermo Fisher Scientific, #11875093) supplemented with 10% heat-inactivated fetal calf serum (FCS) (Sigma/Merck) and 1% Penicillin/Streptomycin (Gibco/Thermo Fisher Scientific). Human endothelial EA.hy926 cells (CRL-2922, ATCC) were maintained in DMEM/F12 (Gibco/Thermo Fisher Scientific). Supplemented with 10% FCS (Sigma/Merck) and 1% Penicillin/Streptomycin (Gibco/Thermo Fisher Scientific).

Establishment of co-culture and triple co-culture models

Transwell inserts (6.5 mm diameter with 5.0 µm pore polycarbonate membrane; Merck Corning, #CLS3421) were coated with 50 µl of 1:1 collagen-fibronectin solution (Collagen I, rat tail #A1048301) and fibronectin (#10838039001, Sigma) from the basal side. The inserts stayed under the hood for air drying. hPMECs were seeded on the basal side of the membranes (cell density: 0.025 x 10^6) and incubated (37°C, 95% humidity, CO_2 concentration of 5%) overnight. Next, hPASMCs were seeded on the apical side of the membranes (cell density: 0.025 x 10^6). With a seeding density of 1:1, an optimal cell proliferation rate was achieved. The cell models were kept in a 1:1 co-culture medium for five days until cell layers were fully confluent, based on barrier integrity evaluation. When co-cultures were established in the microfluidic system, the human monocytic cell line (THP1 cells, density: 0.6 x 10^6) was added to the reservoir facing the hPMECs side of the membrane in a 1:1:1 triple co-culture medium for 8 hours. The culture medium was supplemented with HEPES buffer to maintain a stable pH throughout the experiments.

Apparent permeability

To determine the apparent permeability, we added 200 µL and 500 µL of Fluorescein isothiocyanate dextran (FITC-dextran 4kDa, Sigma Aldrich), and DMEM/F-12, phenol red-free (Thermo Fisher) to the apical (donor) and basal (recipient) compartments, respectively. The basal compartment in a black 96-well plate was sampled every 30 minutes. The culture media was replaced with an equal amount. The samples were analyzed using a plate reader (Safire 2, Tecan) at excitation and emission wavelengths of 483 and 525 nm, respectively. We calculated the apparent permeability coefficient (P_{app}, cm/s) using Equation 2 (51, 52) where dQ/dt is the steady-state flux or the transport rate, A is the surface area of the membrane (0.33 cm^2), and C_0 is the initial concentration of fluorescein sodium added to the apical compartment (mg/mL).

$$P_{app} = \frac{dQ}{dt} * \frac{1}{(A*C_0)} \text{ (Eq. 2).}$$

Transmigration assay

Cell tracker red CMTPX dye (#C34552, Thermo Fisher) was used according to company protocol to monitor the THP1 monocytic cell line movement and location in relation to the hPMECs/hPASMCs co-culture. In brief, the cells were harvested by centrifugation, and the supernatant was aspirated. Afterward, the THP1 monocytic cells were gently resuspended in a pre-warmed CellTrackerTM working solution, resuspended, and incubated for 15-45 minutes under growth conditions. Next, the THP1 monocytic cells were removed from the CellTrackerTM working solution and resuspended in culture media. After loading the THP1 monocytic cells, the dye was well retained, allowing for tracking of cellular movements under the excitation and emission wavelengths of 577⁄602 nm.

Total soluble collagen assay

Total soluble collagen content in total supernatants (co-culture medium) was determined using Sircol™ colorimetric soluble collagen assay (#S1000, Biocolor, UK), according to the manufacturer's instructions.

Nitric oxide assay

Nitric oxide (NO) production was measured in culture medium using Griess assay (#: BML-AK136, Enzo Life Sciences), according to the manufacturer's instructions.

Reactive Oxygen Species (ROS) Assay

ROS levels in the models were measured using the Abcam ROS Assay Kit (ab186027) following the manufacturer's protocol. Briefly, 300 µL of the diluted ROS detection dye was added to each well. After incubation for 30 minutes at room temperature, fluorescence was measured at 520/605 nm using a microplate reader.

Immunofluorescence

For immunofluorescence (IF), samples were fixed with 4% PFA, and incubated at 4°C overnight with primary antibodies CD144 (VE-cadherin) monoclonal Ab (1:100, mouse, #14-1449-82 eBioscience, Invitrogen), cleaved caspase-3 Ab (1:400, rabbit, #9661S, Cell Signaling), Ki67 monoclonal Ab (1:100, mouse, #14-5698-82, eBioscience, Invitrogen), collagen type IV monoclonal Ab (1:100, mouse, #14-9871-82, eBioscience, Invitrogen), followed by secondary antibody incubation overnight. The secondary antibodies were Alexa Fluor 488 goat anti-mouse Ab (1:250, #A-11001, Invitrogen), Alexa Fluor 568 goat anti-mouse Ab (1:250, #A-11004, Invitrogen), Alexa Fluor Plus 488 goat anti-rabbit Ab (1:250, # A32731, Invitrogen), and Alexa Fluor 568 goat anti-rabbit Ab (1:250, #A-11011, Invitrogen). F-actin cytoskeleton and cell nucleus were stained using Alexa Fluor 488 Phalloidin (1:400, #A12379, Invitrogen) and 4′, 6-Diamidino-2-phenylindole (DAPI, 1:1000, # D9542, Sigma-Aldrich), respectively. Samples were embedded in Glycergel DAKO (#S3023, Agilent). Images were acquired using Zeiss 880 upright confocal laser scanning microscopy (CLSM) coupled with ZEN Black 2.3 and processed using the 3D reconstruction ImageJ/Fiji, v 2.3.0/1.53f, National Institutes of Health (NIH), Bethesda, MD, USA (53). IF Images were reconstructed and processed using the 3D IMARIS software (version 9.3.0; Bitplane, Zurich, Switzerland).

3′ Massive Analysis of cDNA Ends (MACE) RNA-sequencing

On each side of the membranes, cells were trypsinized and lysed separately using the Trypsin-EDTA (0.25%) (#25200056, Gibco) and the RLT lysis buffer (#79216, Qiagen) for sample preparation. To ensure high separation efficiency, cell counts and fluorescent staining were performed post-detachment to confirm complete cell detachment. Samples

were stored at -80 ºC and shipped to GenXPro GmbH on dry ice. The process of extraction of RNA from the cells, DNAase digestion, quality control, quantification (Fluorescence photometry, Qbit), cDNA synthesis, and barcoded MACE-Seq library preparation using TrueQuant adaptors and Illumina HiSeq2000 sequencing were done by GenXPro GmbH. Bioinformatic analysis, including raw data cleaning, TrueQuant bias elimination, and quantification for MACE, annotation to existing database entries, gene ontology annotation, and enrichment analysis, was done by GenXPro GmbH.

Animal study

Pathogen-free C57BL/6 mice (male and female) were acquired from Charles River (Sulzfeld, Germany) and housed at constant temperature and humidity, a 12-h light cycle, and food and water ad libitum as described previously (54). After spontaneous delivery, newborn mice [3.3 ± 0.5 g; body weight] were randomly assigned to postnatal treatment on postnatal days 5-7. Following randomization, the pups received oxygen (O_2) with FiO_2 of 0.4 or 0.85 for 8 hours or spontaneously breathed room air ($FiO_2 = 0.21$). Following hyperoxia treatment, neonatal mice were returned to the cage to stay with their mothers for three weeks, i.e., exposure of the neonatal lung to injury was achieved in the saccular stage of lung development (ED 17.5 to postnatal day 5 (P5) in mice; gestational age 27–36 weeks in humans) while lungs were assessed after alveolarization took place. This design was chosen to i) align our *in vivo* studies with clinically relevant conditions and ii) address sustained changes (10, 46). At the age of 26 ± 2 days, lungs were fixed intratracheally with 4% buffered PFA at 20 cmH_2O, and lung volumes were measured as described previously (55), demonstrating comparable results for all groups: FiO_2=0.21: 65± 7.0 μL^3; FiO_2=0.4 group: 66± 5.0 μL^3; FiO_2=0.85 group: 65± 14.0 μL^3 (mean and SD each). All animal experiments followed strict governmental and international guidelines and were approved by the local government for the administrative region of Upper Bavaria Animal Care and Use Committee (TVA no. 55.2-1-54-2532-117-2010). Immunofluorescence staining of the paraffin-embedded lung tissue sections was performed as described previously (54) using F4/80 (#16836155, Thermo Fisher Scientific) and cleaved caspase-3 Ab (1:400, rabbit, #9661S, Cell Signaling). Histology Van Gieson's trichrome staining was performed following the manufacturer's instructions

(Carl Roth, Germany), followed by quantitative and qualitative assessment of microvessels (20-100 µm) as described previously (55). Images were acquired using a Zeiss Axio Scan Z.1 slide scanner (ZEISS).

Statistical analysis

GraphPad Prism 10 for macOS v.10.3.1 (GraphPad Software, CA, USA) was used to analyze the data. The figure legend provides specific details on the statistical analysis and the number of experiments conducted (n). $*p < 0.05$, $**p < 0.001$, and $***p < 0.0001$, $****p < 0.00001$. Differential expression analysis was performed using DESeq2 V.1.36.0 R package with p-value correction by Benjamini-Hochberg. Genes with total counts <10 were discarded, and FDR <0.05 was chosen as the threshold for significance. Enrichment analysis was performed using gProfiler2 V.0.2.1 R package mapping for the Ensembl 109 database (Ensembl Genomes 56, built on 2022-03-29). REACTOME pathways with adjusted p-value < 0.05 (gSCS method, by default) were considered significant. Volcano and bar plots for differential expression and enrichment analysis were created using internal R scripts based on the ggplot2 V.3.4.2 R package. The transcriptomics analysis and visualization scripts were carried out in R V.4.2.3.]

Data Availability

All data generated and analyzed during the current study are available from the corresponding author on request.

Funding

The present study was supported by the Young Investigator Grant NWG VH-NG-829 by the Helmholtz Foundation and the Helmholtz Zentrum Muenchen, Germany, the International Research Group ‘Role of BMP signaling’ (01KI07110), Helmholtz Foundation (Federal Ministry of Education and Research in Germany (BMBF)) and the German Centre for Lung Research (DZL) as well as the Research Training Group ‘Targets in Toxicology’ (GRK2338) of the German Science and Research Organization (DFG). This work was supported by the Deutsche Forschungsgemeinschaft (DFG, German Research Foundation) - TRR 359 - Project number 491676693 and the Chan

Zuckerberg Initiative (Mapping the Pediatric Inhalation Interface: Nose, Mouth, and Airways). Additional financial support was provided by the Stiftung AtemWeg (LSS AIRR). As a member of the PVRI GoDeep Registry (PVRI Global Deep Phenotyping PH Meta-Registry), the study was supported through intellectual contribution. Ali Doryab was supported by the Walter Benjamin Postdoctoral Fellowship from the Deutsche Forschungsgemeinschaft (DFG, German Research Foundation; project number 524039583).

Acknowledgment

The authors would like to thank Andreas Schroeppel, Elisabeth Schindler, and Susanne Mehring for their technical assistance.

Images created with BioRender.com and published with permission.

Author Contributions

Conception and design: MH, AD, and AH.

Methodology and investigation: MH and AD.

Visualization: MH.

Writing – original draft: MH, AD, and AH.

Analysis and interpretation: MH, AD, JH, BS, OS, and AH.

References

1. **Ohuma EO**, **Moller A-B**, **Bradley E**, **Chakwera S**, **Hussain-Alkhateeb L**, **Lewin A**, **Okwaraji YB**, **Mahanani WR**, **Johansson EW**, **Lavin T**, **Fernandez DE**, **Domínguez GG**, **de Costa A**, **Cresswell JA**, **Krasevec J**, **Lawn JE**, **Blencowe H**, **Requejo J**, **Moran AC**. National, regional, and global estimates of preterm birth in 2020, with trends from 2010: a systematic analysis. *The Lancet* 402: 1261–1271, 2023. doi: 10.1016/S0140-6736(23)00878-4.
2. **Jobe AJ**. The New BPD: An Arrest of Lung Development. *Pediatr Res* 46: 641–641, 1999. doi: 10.1203/00006450-199912000-00007.
3. **Sahni M**, **Bhandari V**. Patho-mechanisms of the origins of bronchopulmonary dysplasia. *Mol Cell Pediatr* 8: 21, 2021. doi: 10.1186/s40348-021-00129-5.

4. **Guo X**, **Ma D**, **Li R**, **Zhang R**, **Guo Y**, **Yu Z**, **Chen C**. Association between viral infection and bronchopulmonary dysplasia in preterm infants: a systematic review and meta-analysis. *Eur J Pediatr* 183: 2965–2981, 2024. doi: 10.1007/s00431-024-05565-9.
5. **Course CW**, **Bush A**, **Kotecha S**. Looking beyond bronchopulmonary dysplasia: prematurity-associated lung disease and its phenotypes. *Lancet Respir Med* 14: 60–71, 2026. doi: 10.1016/S2213-2600(25)00372-8.
6. **Hilgendorff A**, **Reiss I**, **Ehrhardt H**, **Eickelberg O**, **Alvira CM**. Chronic Lung Disease in the Preterm Infant. Lessons Learned from Animal Models. *Am J Respir Cell Mol Biol* 50: 233–245, 2014. doi: 10.1165/rcmb.2013-0014TR.
7. **Hansmann G**, **Sallmon H**, **Roehr CC**, **Kourembanas S**, **Austin ED**, **Koestenberger M**. Pulmonary hypertension in bronchopulmonary dysplasia. *Pediatr Res* 89: 446–455, 2021. doi: 10.1038/s41390-020-0993-4.
8. **Häfner F**, **Kindt A**, **Strobl K**, **Förster K**, **Heydarian M**, **Gonzalez E**, **Schubert B**, **Kraus Y**, **Dalla Pozza R**, **Flemmer AW**, **Ertl-Wagner B**, **Dietrich O**, **Stoecklein S**, **Tello K**, **Hilgendorff A**. MRI pulmonary artery flow detects lung vascular pathology in preterms with lung disease. *European Respiratory Journal* 62: 2202445, 2023. doi: 10.1183/13993003.02445-2022.
9. **Giusto K**, **Wanczyk H**, **Jensen T**, **Finck C**. Hyperoxia-induced bronchopulmonary dysplasia: better models for better therapies. *Dis Model Mech* 14, 2021. doi: 10.1242/dmm.047753.
10. **Heydarian M**, **Oak P**, **Zhang X**, **Kamgari N**, **Kindt A**, **Koschlig M**, **Pritzke T**, **Gonzalez-Rodriguez E**, **Förster K**, **Morty RE**, **Häfner F**, **Hübener C**, **Flemmer AW**, **Yildirim AO**, **Sudheendra D**, **Tian X**, **Petrera A**, **Kirsten H**, **Ahnert P**, **Morrell N**, **Desai TJ**, **Sucre J**, **Spiekerkoetter E**, **Hilgendorff A**. Relationship between impaired BMP signalling and clinical risk factors at early-stage vascular injury in the preterm infant. *Thorax* 77: 1176–1186, 2022. doi: 10.1136/thoraxjnl-2021-218083.
11. **Cool CD**, **Kuebler WM**, **Bogaard HJ**, **Spiekerkoetter E**, **Nicolls MR**, **Voelkel NF**. The hallmarks of severe pulmonary arterial hypertension: the cancer hypothesis—ten years later. *American Journal of Physiology-Lung Cellular and Molecular Physiology* 318: L1115–L1130, 2020. doi: 10.1152/ajplung.00476.2019.
12. **Mourani PM**, **Abman SH**. Pulmonary vascular disease in bronchopulmonary dysplasia. *Curr Opin Pediatr* 25: 329–337, 2013. doi: 10.1097/MOP.0b013e328360a3f6.
13. **Wang H**, **Jafri A**, **Martin RJ**, **Nnanabu J**, **Farver C**, **Prakash YS**, **MacFarlane PM**. Severity of neonatal hyperoxia determines structural and functional changes in developing mouse airway. *American Journal of Physiology-Lung Cellular and Molecular Physiology* 307: L295–L301, 2014. doi: 10.1152/ajplung.00208.2013.
14. **Attaye I**, **Smulders YM**, **de Waard MC**, **Oudemans-van Straaten HM**, **Smit B**, **Van Wijhe MH**, **Musters RJ**, **Koolwijk P**, **Spoelstra–de Man AME**. The effects of hyperoxia on microvascular endothelial cell proliferation and production of vaso-active substances. *Intensive Care Med Exp* 5: 22, 2017. doi: 10.1186/s40635-017-0135-4.
15. **D'Amore PA**, **Sweet E**. Effects of hyperoxia on microvascular cells in vitro. *In Vitro Cellular & Developmental Biology* 23: 123–128, 1987. doi: 10.1007/BF02623592.
16. **Yang W**, **Dong M**, **Rabinovitch M**, **Chan FP**, **Marsden AL**, **Feinstein JA**. Evolution of hemodynamic forces in the pulmonary tree with progressively worsening pulmonary arterial hypertension in pediatric patients. *Biomech Model Mechanobiol* 18: 779–796, 2019. doi: 10.1007/s10237-018-01114-0.

17. **Kostyunina DS**, **Rowan SC**, **Pakhomov N V.**, **Dillon E**, **Rochfort KD**, **Cummins PM**, **O'Rourke MJ**, **McLoughlin P**. Shear Stress Markedly Alters the Proteomic Response to Hypoxia in Human Pulmonary Endothelial Cells. *Am J Respir Cell Mol Biol* 68: 551–565, 2023. doi: 10.1165/rcmb.2022-0340OC.
18. **Windhorst AC**, **Heydarian M**, **Schwarz M**, **Oak P**, **Förster K**, **Frankenberger M**, **Gonzalez Rodriguez E**, **Zhang X**, **Ehrhardt H**, **Hübener C**, **Flemmer AW**, **Hossain H**, **Stoeger T**, **Schulz C**, **Hilgendorff A**. Monocyte signature as a predictor of chronic lung disease in the preterm infant. *Front Immunol* 14: 1–9, 2023. doi: 10.3389/fimmu.2023.1112608.
19. **Heydarian M**, **Schulz C**, **Stoeger T**, **Hilgendorff A**. Association of immune cell recruitment and BPD development. *Mol Cell Pediatr* 9: 16, 2022. doi: 10.1186/s40348-022-00148-w.
20. **Schermuly RT**, **Ghofrani HA**, **Wilkins MR**, **Grimminger F**. Mechanisms of disease: pulmonary arterial hypertension. *Nat Rev Cardiol* 8: 443–455, 2011. doi: 10.1038/nrcardio.2011.87.
21. **Balink S**, **Onland W**, **Vrijlandt EJLE**, **Andrinopoulou E-R**, **Bos AF**, **Dijk PH**, **Goossens L**, **Hulsmann AR**, **Nuytemans DH**, **Reiss IKM**, **Sprij AJ**, **Kroon AA**, **van Kaam AH**, **Pijnenburg M**. Supplemental oxygen strategies in infants with bronchopulmonary dysplasia after the neonatal intensive care unit period: study protocol for a randomised controlled trial (SOS BPD study). *BMJ Open* 12: e060986, 2022. doi: 10.1136/bmjopen-2022-060986.
22. **Enomoto M**, **Gosal K**, **Cubells E**, **Escobar J**, **Vento M**, **Jankov RP**, **Belik J**. Sex-dependent changes in the pulmonary vasoconstriction potential of newborn rats following short-term oxygen exposure. *Pediatr Res* 72: 468–478, 2012. doi: 10.1038/pr.2012.120.
23. **Mourani PM**, **Abman SH**. Pulmonary Hypertension and Vascular Abnormalities in Bronchopulmonary Dysplasia. *Clin Perinatol* 42: 839–855, 2015. doi: 10.1016/j.clp.2015.08.010.
24. **Häfner F**, **Kindt A**, **Strobl K**, **Förster K**, **Heydarian M**, **Gonzalez E**, **Schubert B**, **Kraus Y**, **Robert DP**, **Flemmer AW**, **Ertl-Wagner B**, **Dietrich O**, **Stoecklein S**, **Tello K**, **Hilgendorff A**. MRI pulmonary artery flow detects lung vascular pathology in preterms with lung disease. .
25. **Puchwein-Schwepcke A**, **Grzybowski A-K**, **Genzel-Boroviczény O**, **Nussbaum C**. Effects of Prematurity on the Cutaneous Microcirculatory Network in the First Weeks of Life. *Front Pediatr* 7: 1–9, 2019. doi: 10.3389/fped.2019.00198.
26. **Doryab A**, **Schmid O**. Towards a gold standard functional readout to characterize In Vitro lung barriers. *European Journal of Pharmaceutical Sciences* 179: 106305, 2022. doi: 10.1016/j.ejps.2022.106305.
27. **Malikova E**, **Kmecova Z**, **Doka G**, **Pivackova LB**, **Balis P**, **Trubacova S**, **Velasova E**, **Krenek P**, **Klimas J**. Pioglitazone restores phosphorylation of downregulated caveolin-1 in right ventricle of monocrotaline-induced pulmonary hypertension. *Clin Exp Hypertens* 44: 101–112, 2022. doi: 10.1080/10641963.2021.1996589.
28. **Nakano N**, **Sakata N**, **Katsu Y**, **Nochise D**, **Sato E**, **Takahashi Y**, **Yamaguchi S**, **Haga Y**, **Ikeno S**, **Motizuki M**, **Sano K**, **Yamasaki K**, **Miyazawa K**, **Itoh S**. Dissociation of the AhR/ARNT complex by TGF-β/Smad signaling represses CYP1A1 gene expression and inhibits benze[a]pyrene-mediated cytotoxicity. *Journal of Biological Chemistry* 295: 9033–9051, 2020. doi: 10.1074/jbc.RA120.013596.

29. **Patil MN**, **Datkhile KD**, **Gudur AK**, **Gudur RA**, **Patil SR**. Single-nucleotide polymorphism in CYP1A1, CYP1B1, CYP2B6, CYP2C8, and CYP2C9 genes and their association with gastrointestinal cancer: A hospital-based case-control study. *J Cancer Res Ther* 20: 216–223, 2024. doi: 10.4103/jcrt.jcrt_294_22.
30. **Higuchi Y**, **Ogata T**, **Nakanishi N**, **Nishi M**, **Tsuji Y**, **Tomita S**, **Conway SJ**, **Matoba S**. Cavin-2 promotes fibroblast-to-myofibroblast trans-differentiation and aggravates cardiac fibrosis. *ESC Heart Fail* 11: 167–178, 2024. doi: 10.1002/ehf2.14571.
31. **Ramirez A**, **Vyzas CA**, **Zhao H**, **Eng K**, **Degenhardt K**, **Astrof S**. Buffering Mechanism in Aortic Arch Artery Formation and Congenital Heart Disease. *Circ Res* 134, 2024. doi: 10.1161/CIRCRESAHA.123.322767.
32. **Lin X**, **Liu W**, **Chu Y**, **Zhang H**, **Zeng L**, **Lin Y**, **Kang K**, **Peng F**, **Lin J**, **Huang C**, **Chai D**. Activation of AHR by ITE improves cardiac remodelling and function in rats after myocardial infarction. *ESC Heart Fail* 10: 3622–3636, 2023. doi: 10.1002/ehf2.14532.
33. **Moon J**, **Zhou H**, **Zhang L**, **Tan W**, **Liu Y**, **Zhang S**, **Morlock LK**, **Bao X**, **Palecek SP**, **Feng JQ**, **Williams NS**, **Amatruda JF**, **Olson EN**, **Bassel-Duby R**, **Lum L**. Blockade to pathological remodeling of infarcted heart tissue using a porcupine antagonist. *Proceedings of the National Academy of Sciences* 114: 1649–1654, 2017. doi: 10.1073/pnas.1621346114.
34. **Giusto K**, **Wanczyk H**, **Jensen T**, **Finck C**. Hyperoxia-induced bronchopulmonary dysplasia: better models for better therapies. *Dis Model Mech* 14, 2021. doi: 10.1242/dmm.047753.
35. **Kapadia V**, **Oei JL**. Optimizing oxygen therapy for preterm infants at birth: Are we there yet? *Semin Fetal Neonatal Med* 25: 101081, 2020. doi: 10.1016/j.siny.2020.101081.
36. **Welsford M**, **Nishiyama C**, **Shortt C**, **Weiner G**, **Roehr CC**, **Isayama T**, **Dawson JA**, **Wyckoff MH**, **Rabi Y**. Initial Oxygen Use for Preterm Newborn Resuscitation: A Systematic Review With Meta-analysis. *Pediatrics* 143: 1–17, 2019. doi: 10.1542/peds.2018-1828.
37. **Kumar VHS**, **Wang H**, **Nielsen L**. Short-term perinatal oxygen exposure may impair lung development in adult mice. *Biol Res* 53: 51, 2020. doi: 10.1186/s40659-020-00318-y.
38. **Vogel ER**, **Britt RD**, **Faksh A**, **Kuipers I**, **Pandya H**, **Prakash YS**, **Martin RJ**, **Pabelick CM**. Moderate hyperoxia induces extracellular matrix remodeling by human fetal airway smooth muscle cells. *Pediatr Res* 81: 376–383, 2017. doi: 10.1038/pr.2016.218.
39. **Twisselmann N**, **Pagel J**, **Künstner A**, **Weckmann M**, **Hartz A**, **Glaser K**, **Hilgendorff A**, **Göpel W**, **Busch H**, **Herting E**, **Weinberg JB**, **Härtel C**. Hyperoxia/Hypoxia Exposure Primes a Sustained Pro-Inflammatory Profile of Preterm Infant Macrophages Upon LPS Stimulation. *Front Immunol* 12: 1–20, 2021. doi: 10.3389/fimmu.2021.762789.
40. **San Sebastián-Jaraba I**, **Fernández-Gómez MJ**, **Blázquez-Serra R**, **Sanz-Andrea S**, **Blanco-Colio LM**, **Méndez-Barbero N**. In vitro 3D co-culture model of human endothelial and smooth muscle cells to study pathological vascular remodeling. *Clínica e Investigación en Arteriosclerosis (English Edition)* 36: 356–363, 2024. doi: 10.1016/j.artere.2024.11.004.
41. **Boehme J**, **Sun X**, **Tormos K V.**, **Gong W**, **Kellner M**, **Datar SA**, **Kameny RJ**, **Yuan JX-J**, **Raff GW**, **Fineman JR**, **Black SM**, **Maltepe E**. Pulmonary artery smooth muscle cell hyperproliferation and metabolic shift triggered by pulmonary overcirculation. *American Journal of Physiology-Heart and Circulatory Physiology* 311: H944–H957, 2016. doi: 10.1152/ajpheart.00040.2016.

42. **Morii C**, **Tanaka HY**, **Izushi Y**, **Nakao N**, **Yamamoto M**, **Matsubara H**, **Kano MR**, **Ogawa A**. 3D in vitro Model of Vascular Medial Thickening in Pulmonary Arterial Hypertension. *Front Bioeng Biotechnol* 8, 2020. doi: 10.3389/fbioe.2020.00482.
43. **Lavender MD**, **Pang Z**, **Wallace CS**, **Niklason LE**, **Truskey GA**. A system for the direct co-culture of endothelium on smooth muscle cells. *Biomaterials* 26: 4642–4653, 2005. doi: 10.1016/j.biomaterials.2004.11.045.
44. **Conhaim RL**, **Segal GS**, **Watson KE**. Positive pressure ventilation compresses pulmonary acinar microvessels but not their supply vessels. *Microvasc Res* 122: 71–77, 2019. doi: 10.1016/j.mvr.2018.11.008.
45. **Doryab A**, **Groll J**. Biomimetic In Vitro Lung Models: Current Challenges and Future Perspective. *Advanced Materials* 35, 2023. doi: 10.1002/adma.202210519.
46. **Hussain M**, **Xu C**, **Ahmad M**, **Yang Y**, **Lu M**, **Wu X**, **Tang L**, **Wu X**. Notch Signaling: Linking Embryonic Lung Development and Asthmatic Airway Remodeling. *Mol Pharmacol* 92: 676–693, 2017. doi: 10.1124/mol.117.110254.
47. **Vis MAM**, **Ito K**, **Hofmann S**. Impact of Culture Medium on Cellular Interactions in in vitro Co-culture Systems. *Front Bioeng Biotechnol* 8, 2020. doi: 10.3389/fbioe.2020.00911.
48. **Meyer S**, **Bay J**, **Franz AR**, **Erhardt H**, **Klein L**, **Petzinger J**, **Binder C**, **Kirschenhofer S**, **Stein A**, **Hüning B**, **Heep A**, **Cloppenburg E**, **Muyimbwa J**, **Ott T**, **Sandkötter J**, **Teig N**, **Wiegand S**, **Schroth M**, **Kick A**, **Wurm D**, **Gebauer C**, **Linnemann K**, **Kittel J**, **Wieg C**, **Kiechl-Kohlendorfer U**, **Schmidt S**, **Böttger R**, **Thomas W**, **Brevis Nunez F**, **Stockmann A**, **Kriebel T**, **Müller A**, **Klotz D**, **Morhart P**, **Nohr D**, **Biesalski HK**, **Giannopoulou EZ**, **Hilt S**, **Poryo M**, **Wagenpfeil S**, **Haiden N**, **Ruckes C**, **Ehrlich A**, **Gortner L**, **Schuler R**, **Kampschulte B**, **Schmidt A**, **Atanasov S**, **Dzietko M**, **Prager S**, **Bialas I**, **Kramps P**, **Beckmann S**, **Seidenberg J**, **Majosthusmann K**, **Potratz J**, **van den Heuvel A**, **Tekaat M**, **Dettmers S**, **Unterweger M-T**, **Nowak H**, **Möller J**, **Thome U**, **Arand J**, **Luger B**, **Maiwald CA**, **Heideking M**, **Heckmann M**, **Keller-Wacherbauer A**, **Michel H**, **Karen T**, **Schmid A**, **Pellkofer Y**, **Griesmaier E**, **Genzel-Boroviczeny O**, **Mata Fernandez R**, **Avenarius S**, **Czoske A**, **Block C**, **Schwarz S**, **Jenke A**, **Grass T**, **Kuntz M**, **Fahlbusch F**, **Pöschl J**, **Metzger J**, **Ronellenfitsch S**, **Schaible T**, **Reinhard J**, **Trepels-Kottek S**, **Bauer J**, **Herting E**, **Henn W**, **Laupert A**, **Jathe R**. Early postnatal high-dose fat-soluble enteral vitamin A supplementation for moderate or severe bronchopulmonary dysplasia or death in extremely low birthweight infants (NeoVitaA): a multicentre, randomised, parallel-group, double-blind, placebo-controlled. investigator-initiated phase 3 trial. *Lancet Respir Med* 12, 2024. doi: 10.1016/S2213-2600(24)00073-0.
49. **Häfner F**, **Johansson C**, **Schwarzkopf L**, **Förster K**, **Kraus Y**, **Flemmer AW**, **Hansmann G**, **Sallmon H**, **Felderhoff-Müser U**, **Witt S**, **Schwettmann L**, **Hilgendorff A**. Current diagnosis and treatment practice for pulmonary hypertension in bronchopulmonary dysplasia—A survey study in Germany (PUsH BPD). *Pulm Circ* 13, 2023. doi: 10.1002/pul2.12320.
50. **Poon C**. Measuring the density and viscosity of culture media for optimized computational fluid dynamics analysis of in vitro devices. *J Mech Behav Biomed Mater* 126: 105024, 2022. doi: 10.1016/j.jmbbm.2021.105024.
51. **Doryab A**, **Taskin MB**, **Stahlhut P**, **Groll J**, **Schmid O**. Real-Time Measurement of Cell Mechanics as a Clinically Relevant Readout of an In Vitro Lung Fibrosis Model Established on a Bioinspired Basement Membrane. *Advanced Materials* 34, 2022. doi: 10.1002/adma.202205083.

52. **Hubatsch I**, **Ragnarsson EGE**, **Artursson P**. Determination of drug permeability and prediction of drug absorption in Caco-2 monolayers. *Nat Protoc* 2: 2111–2119, 2007. doi: 10.1038/nprot.2007.303.
53. **Schindelin J**, **Arganda-Carreras I**, **Frise E**, **Kaynig V**, **Longair M**, **Pietzsch T**, **Preibisch S**, **Rueden C**, **Saalfeld S**, **Schmid B**, **Tinevez J-Y**, **White DJ**, **Hartenstein V**, **Eliceiri K**, **Tomancak P**, **Cardona A**. Fiji: an open-source platform for biological-image analysis. *Nat Methods* 9: 676–682, 2012. doi: 10.1038/nmeth.2019.
54. **Heydarian M**, **Oak P**, **Zhang X**, **Kamgari N**, **Kindt A**, **Koschlig M**, **Pritzke T**, **Gonzalez-Rodriguez E**, **Förster K**, **Morty RE**, **Häfner F**, **Hübener C**, **Flemmer AW**, **Yildirim AO**, **Sudheendra D**, **Tian X**, **Petrera A**, **Kirsten H**, **Ahnert P**, **Morrell N**, **Desai TJ**, **Sucre J**, **Spiekerkoetter E**, **Hilgendorff A**. Relationship between impaired BMP signalling and clinical risk factors at early-stage vascular injury in the preterm infant. *Thorax* 77: 1176–1186, 2022. doi: 10.1136/thoraxjnl-2021-218083.
55. **Oak P**, **Pritzke T**, **Thiel I**, **Koschlig M**, **Mous DS**, **Windhorst A**, **Jain N**, **Eickelberg O**, **Foerster K**, **Schulze A**, **Goepel W**, **Reicherzer T**, **Ehrhardt H**, **Rottier RJ**, **Ahnert P**, **Gortner L**, **Desai TJ**, **Hilgendorff A**. Attenuated PDGF signaling drives alveolar and microvascular defects in neonatal chronic lung disease . *EMBO Mol Med* 9: 1504–1520, 2017. doi: 10.15252/emmm.201607308.

Figure legends:

Figure 1. Concept and characterization of the biomimetic pulmonary *in vitro* perfusion (PIPE) system for investigating shear stress and oxygen exposure as a model of pulmonary vascular disease (PVD).

(A) Schematic of the PIPE platform, consisting of a main chamber and an external medium reservoir connected in a closed perfusion loop. Cell culture inserts are housed within the main chamber, where culture medium is continuously perfused using a peristaltic pump to apply controlled shear stress to the basal surface of the cell model. All cells were maintained in fully submerged conditions. The apical compartment is connected to an air-tight container that enables precise control of temperature, humidity, and oxygen concentration. (B) Representative photograph of the multiwell PIPE system, showing both the main chambers and the external reservoirs.

(C) Computational modeling of shear stress within the main chamber. (i) Schematic of the Transwell-based flow channel used for simulations. (ii) Simulated velocity profile across the channel. (iii) Line profile of wall shear stress (WSS) at the endothelial cell surface. Simulations were performed using the following parameters: flow rate 2 mL/min, channel length 6.5 mm, channel height 0.4 mm. The resulting WSS was ~1.09 Pa (10.9 dyn/cm^2). Flow was generated using a peristaltic pump, resulting in quasi-continuous flow with inherent low-amplitude pulsatility. (D) Immunofluorescence images of EA.hy926 endothelial monolayers cultured on the bottom (basal) side of the Transwell insert and exposed to 24 h of shear stress, demonstrating alignment of the F-actin cytoskeleton

(green) in the direction of flow. Nuclei are stained with DAPI (blue). (E) Workflow for establishing the PIPE co-culture model using primary human pulmonary microvascular endothelial cells (hPMECs; basal side) and primary human pulmonary arterial smooth muscle cells (hPASMCs; apical side), expanded to confluence over 5 days. (F) Confocal laser scanning microscopy (CLSM) images of the co-culture model. XZ reconstruction (left) shows VE-cadherin (red) localized at endothelial cell junctions on the basal surface, and XY view (right) shows hPASMC organization on the apical surface. F-actin is stained with phalloidin (green), and nuclei with DAPI (blue). Scale bar: 50 µm.
(G) Time-dependent measurements of apparent permeability (P_{app}, FITC-dextran 4 kDa) demonstrating formation of the endothelial/SMC barrier (mean ± SD, n = 6). Statistical analysis was performed using one-way ANOVA with Tukey's post hoc test; *p < 0.05, ****p < 0.0001, ns: not significant.

Figure 2. Comparative effects of dynamic shear stress versus static culture on cellular responses.
(A) CLSM images of the co-culture model showing F-actin cytoskeleton (phalloidin, green) and nuclei (DAPI, blue) on both the apical (hPASMC) and basal (hPMEC) surfaces. The basal endothelial layer additionally shows VE-cadherin (red) and Ki67 (magenta) staining. Scale bar: 50 µm. (B-C) Quantification of endothelial cell proliferation ($Ki67^+$ cells, magenta) (B) and apparent permeability (P_{app}) (C) under static versus dynamic shear stress (10.9 dyn/cm^2, 8 h). (D-E) Analysis of nitrite secretion (D, measured by Griess assay and total soluble collagen content (E) in co-culture models exposed to static or dynamic conditions. (F) Transcriptomic profiling of shear stress-exposed co-cultures using 3' massive analysis of cDNA ends (MACE) RNA sequencing. Volcano plots (left) display differentially expressed genes in (i) hPASMCs (apical side) and (ii) hPMECs (basal side), with upregulated genes shown in green and downregulated genes in yellow. Box plots (right) summarize mean expression levels of the top five significantly enriched biological pathways (upregulated and downregulated) in hPASMCs (P < 0.05, n = 3). (G) Schematic of the triple co-culture setup in which THP-1 monocytic cells were added to the basal compartment of the hPMEC/hPASMC co-culture and exposed to either static or shear stress conditions for 8 h. (H) Surface-rendered immunofluorescence images of the triple co-culture model showing transmigration of THP-1 monocytes (red) from the basal endothelial layer toward the apical smooth muscle layer. Scale bar: 50 µm. (I) Quantification of transmigrated THP-1 monocytes. Data are presented as mean ± SD (n = 5) and were analyzed using an unpaired t-test. *p < 0.05, **p < 0.01.

Figure 3. Effects of distinct oxygen concentrations on cell behavior under dynamic culture conditions.

(A) Schematic of the triple co-culture system (hPMECs/hPASMCs/THP-1) exposed to static or shear stress conditions and three oxygen environments: (21% O_2), moderate hyperoxia (40% O_2), and severe hyperoxia (85% O_2). (B-D) Evaluation of barrier function and oxidative stress responses. (B) Apparent permeability**,** (C) Intracellular reactive oxygen species (ROS) levels. (D) Orthogonal immunofluorescence confocal images of the triple co-culture model showing F-actin (phalloidin, green), nuclei (DAPI, blue), and CMTPX-labeled THP-1 monocytes (red). Scale bar: 50 µm. (E) Quantification of THP-1 monocytic cell movement and localization within the hPMEC/hPASMC co-culture, tracked using CellTracker™ Red CMTPX. (F-H) Immunofluorescence Z-projection images showing qualitative (F) and quantitative (G) analysis of caspase-3 (red), and (H) collagen IV (magenta) expression within the triple co-culture model. Scale bar: 50 µm. (I) Total soluble collagen content measured in culture supernatants. Data are presented as mean ± SD (n = 5) and analyzed using two-way ANOVA with Tukey's multiple comparisons test. *p < 0.05, **p < 0.01, ***p < 0.001.

Figure 4. *In vivo* evaluation of moderate and severe hyperoxia-induced lung injury.

(A) Schematic of the neonatal mouse model in which neonatal mice were exposed for 8 h to room air (normoxia), moderate hyperoxia (FiO_2 = 0.40; 40% O_2), or severe hyperoxia (FiO_2 = 0.85; 85% O_2) to induce acute lung injury. (B) Quantification of pulmonary microvessel density (20-100 µm diameter) in lung tissue sections. (C-D) Representative immunofluorescence images showing macrophage infiltration (F4/80, C) and apoptotic activity (caspase-3, D). Scale bars: 50 µm. (E) Qualitative and quantitative analysis of collagen deposition using Van Gieson staining, where collagen fibers appear pink, nuclei dark brown, and cytoplasm yellow. Scale bar: 500 µm. Data are presented as mean ± SD (n = 5) and were analyzed using one-way ANOVA with Tukey's multiple comparisons test. *p < 0.05, **p < 0.01, ***p < 0.001.

A

Pulmonary *In vitro* **PE**rfusion (**PIPE**) system

Air-tight container filled with specified Oxygen concentration

Oxygen meter

Oxygen outlet

Filter

Reservoir

Main Chamber

Peristaltic pump

Smooth muscle cells

Inlet flow

Channel height: 0.4 mm

Endothelial layer

B

Multiwell PIPE system in the lab (main and external chambers)

C

(i)

Membrane

Endothelial cell monolayer (shear applied here)

Inlet flow

Height 0.4 mm

Outlet flow

Channel length :6.5 mm

(ii)

Velocity magnitude [m/s]

×10⁻⁴ m

[m/s]

0.12

0.1

0.08

0.06

0.04

0.02

0

Channel height [m]

Channel length [m]

(iii)

Wall Shear Stress (Pa)

[Pa]

34

32.3

30.6

28.8

27.1

25.3

23.6

21.8

20.1

18.3

16.6

14.8

13.1

11.4

9.62

7.87

6.12

4.38

2.63

0.89

1.09 Pa

(10.9 dyne/cm²)

D

F-actin DAPI

After 24 h Shear stress

E

Day 0

Basal seeding

Human pulmonary microvascular endothelial cells (HPMECs)

Day 1

Apical seeding

Human primary pulmonary arterial smooth muscle cells (HPASMCs)

Day 5

Growth to confluence

Basal (HMPECs) *VE-Cadherin DAPI*

Apical (HPASMCs) *F-actin DAPI*

F

Cross-sectional (confocal z-stack)

Apical

Basal

G

****

*

ns

Papp (cm/s)

1×10⁻⁵

8×10⁻⁶

6×10⁻⁶

4×10⁻⁶

2×10⁻⁶

0

1

3

5

6

Time (day)

A

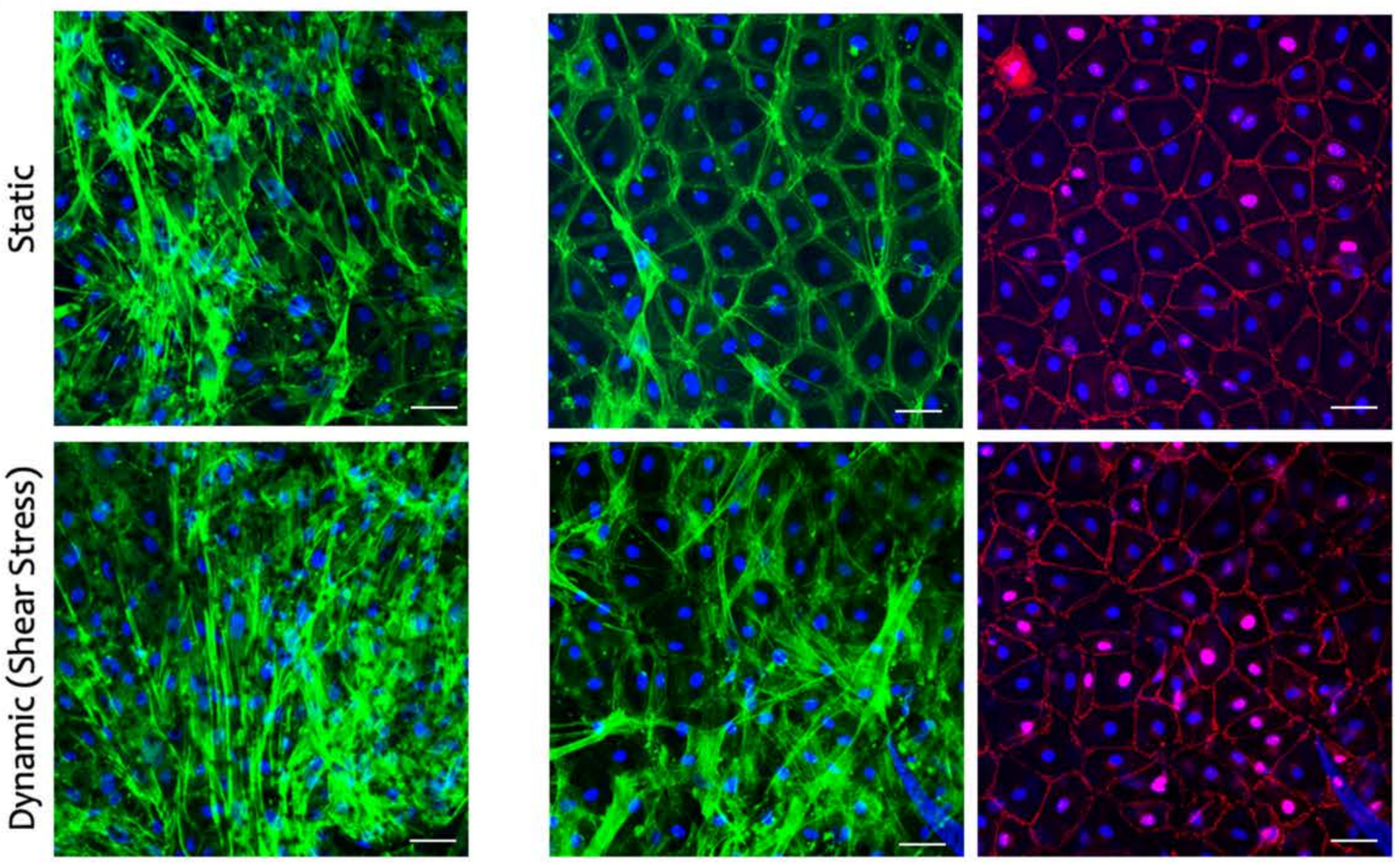

B

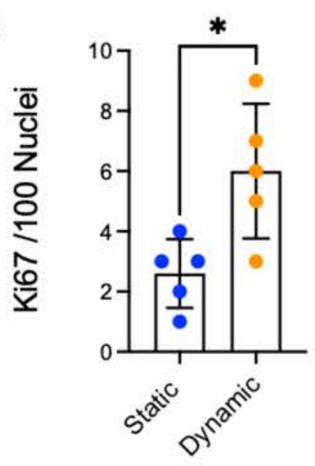

C

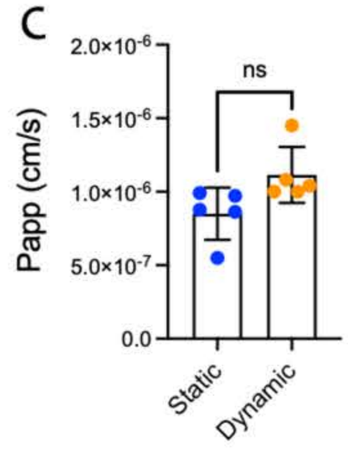

D

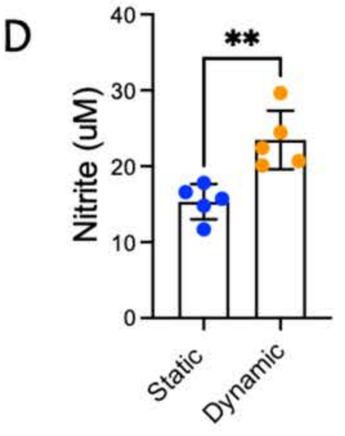

E

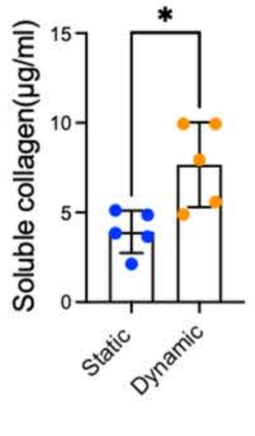

F

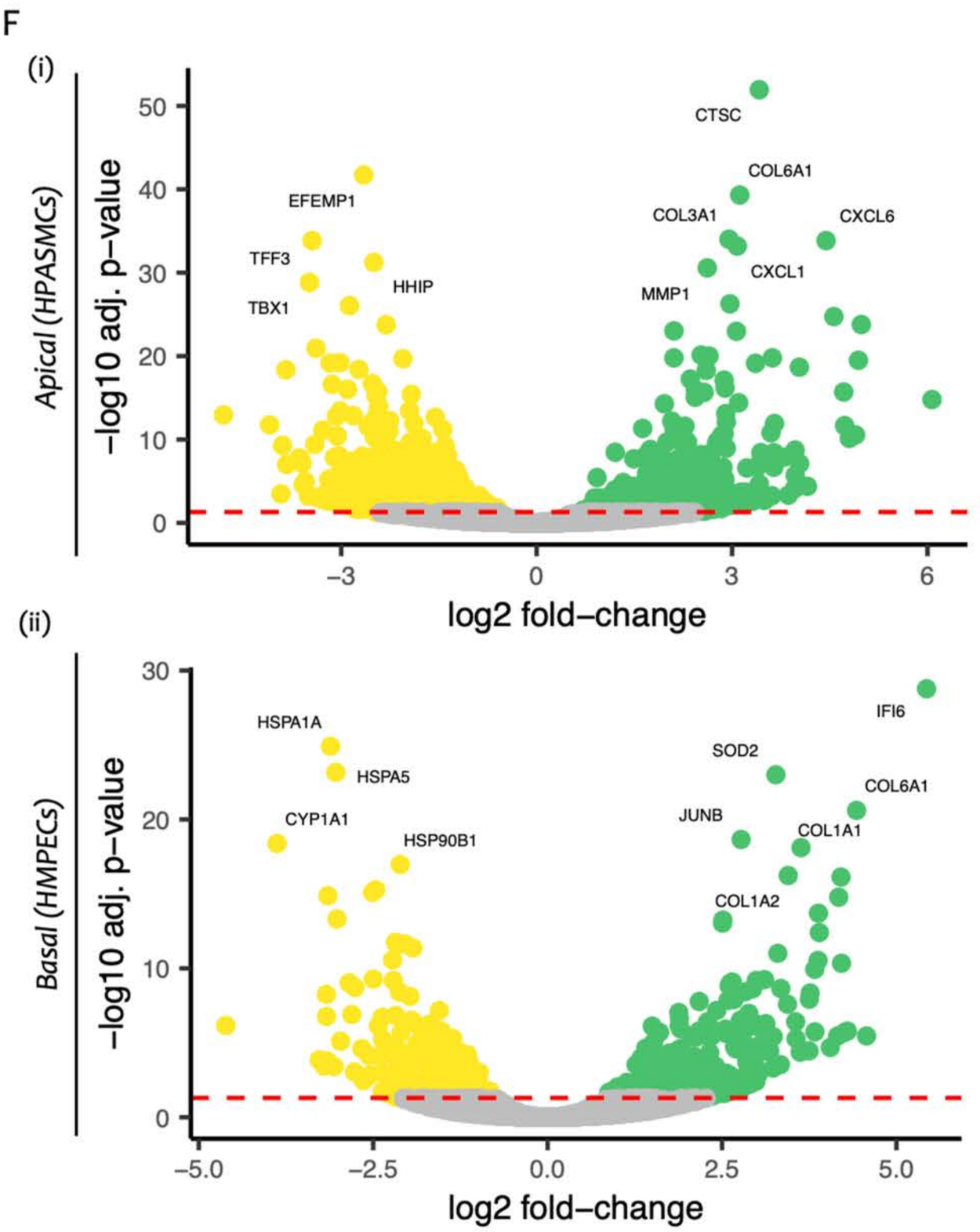

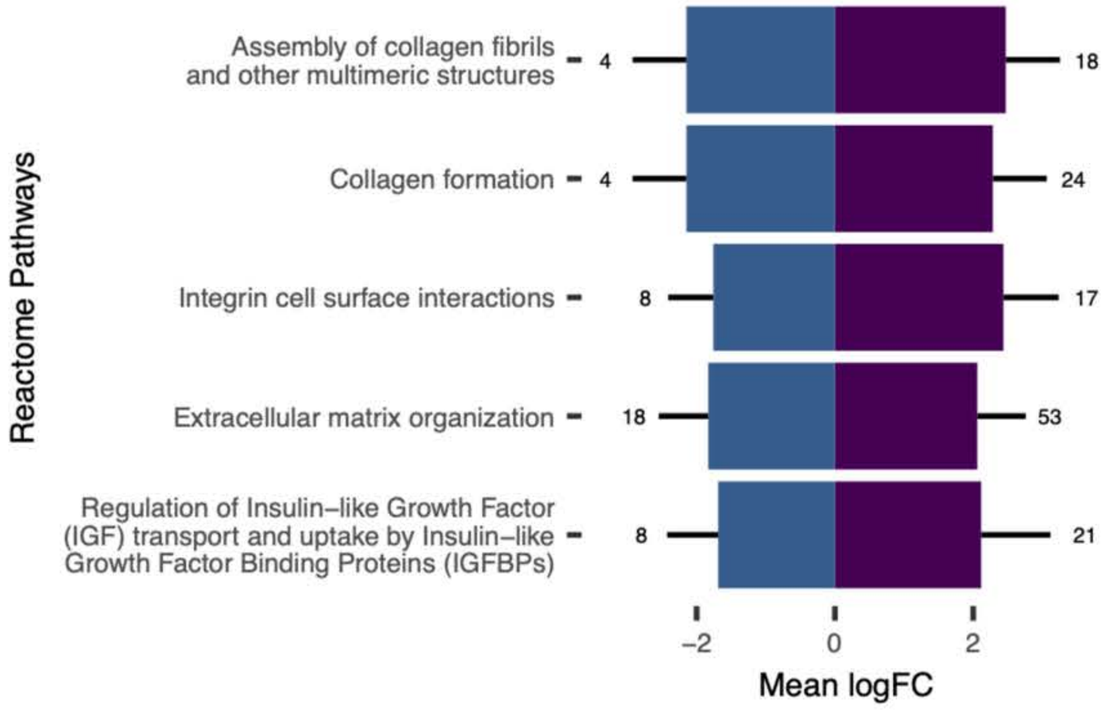

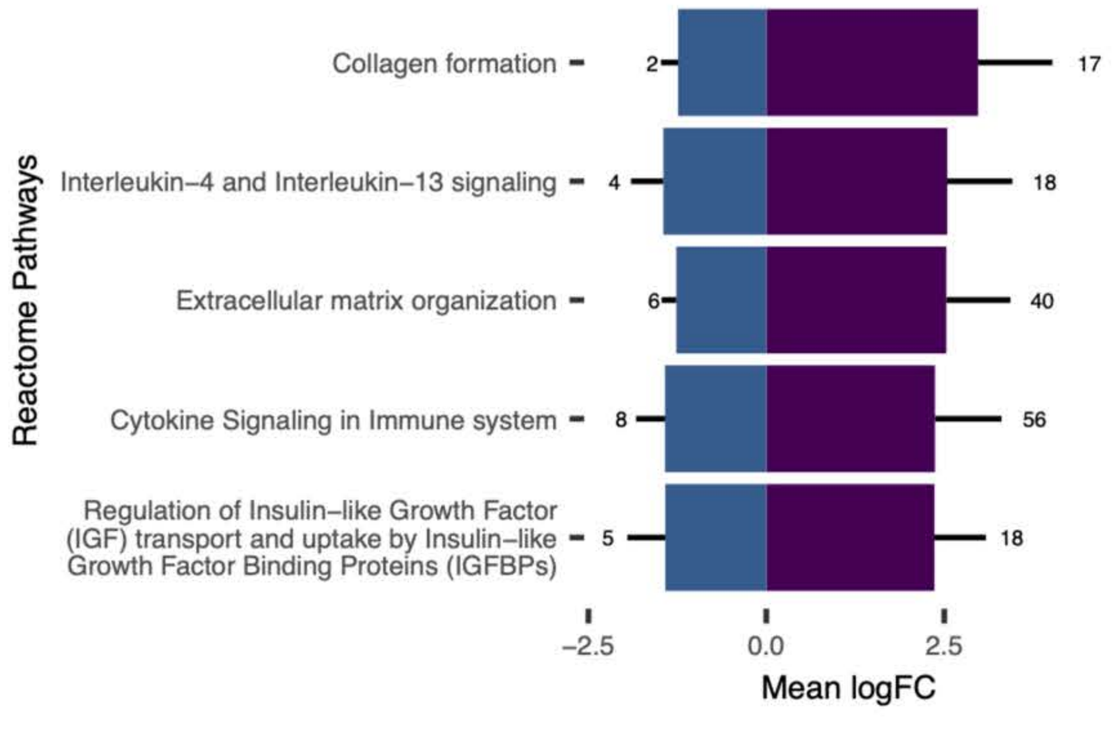

G

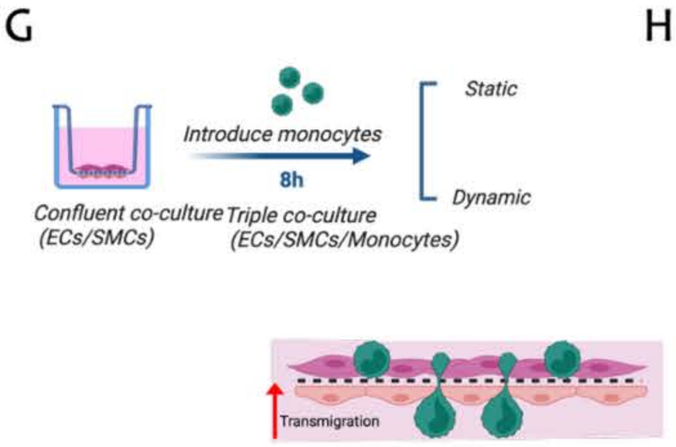

H

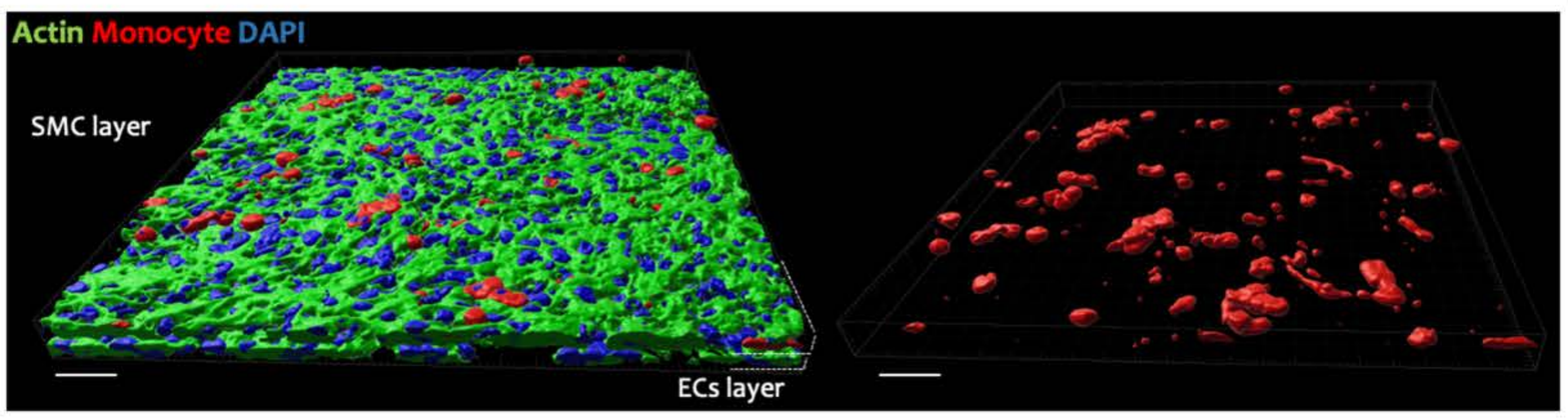

I

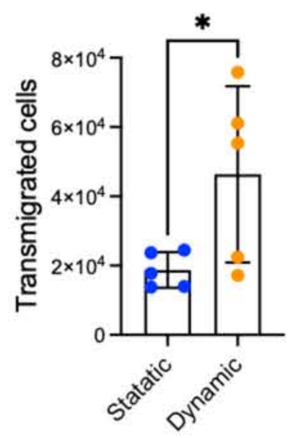

A

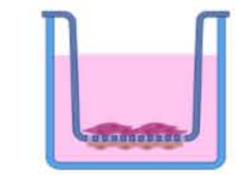

Confluent co-culture
(ECs/SMCs)

Introduce monocytes

Dynamic 8h

Triple co-culture
(ECs/SMCs/Monocytes)

Normoxia
(21% Oxygen)

Hyperoxia
(40% Oxygen)

Hyperoxia
(85% Oxygen)

B

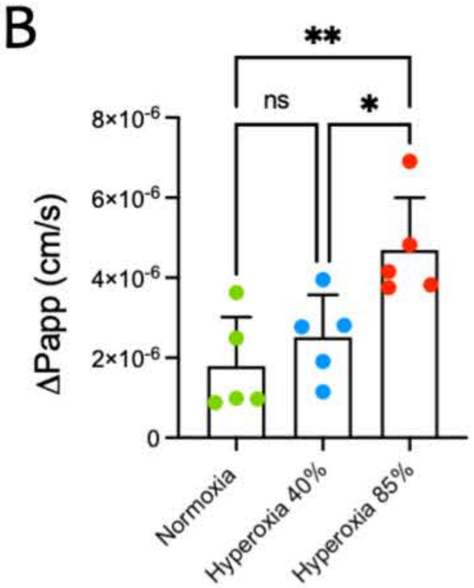

C

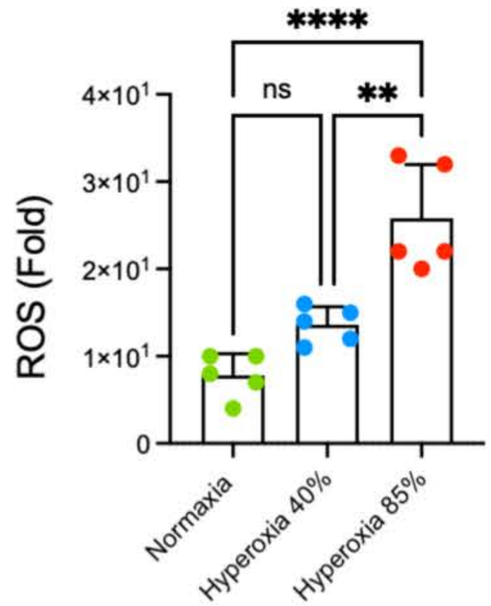

D

Normoxia

Hyperoxia 40%

Hyperoxia 85%

Apical side

THP1 F-actin DAPI

XZ

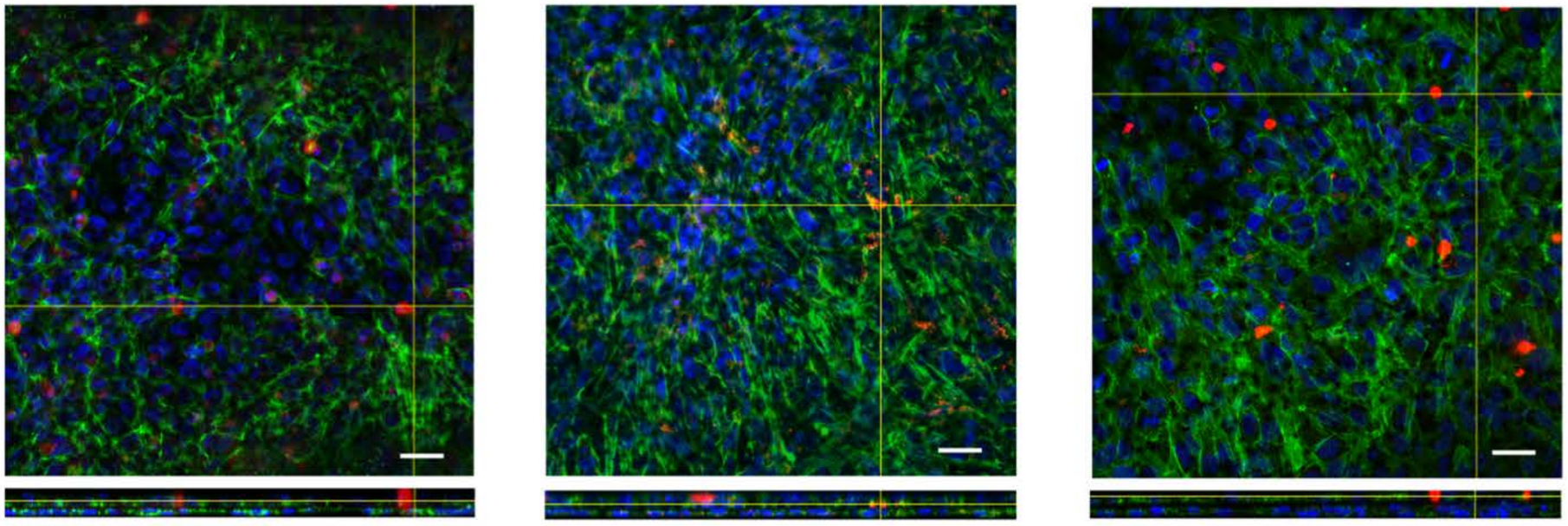

E

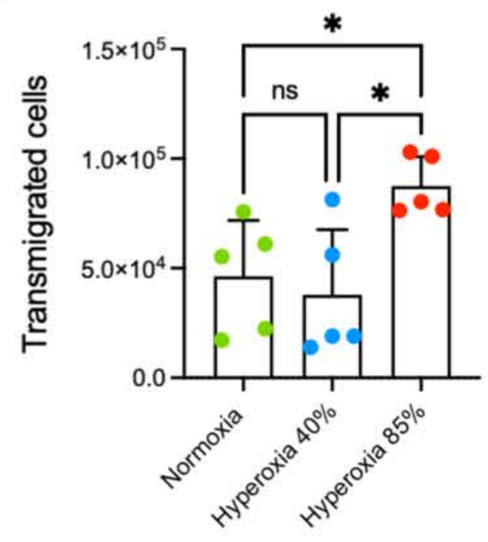

F

Z-projection

Caspase3 DAPI

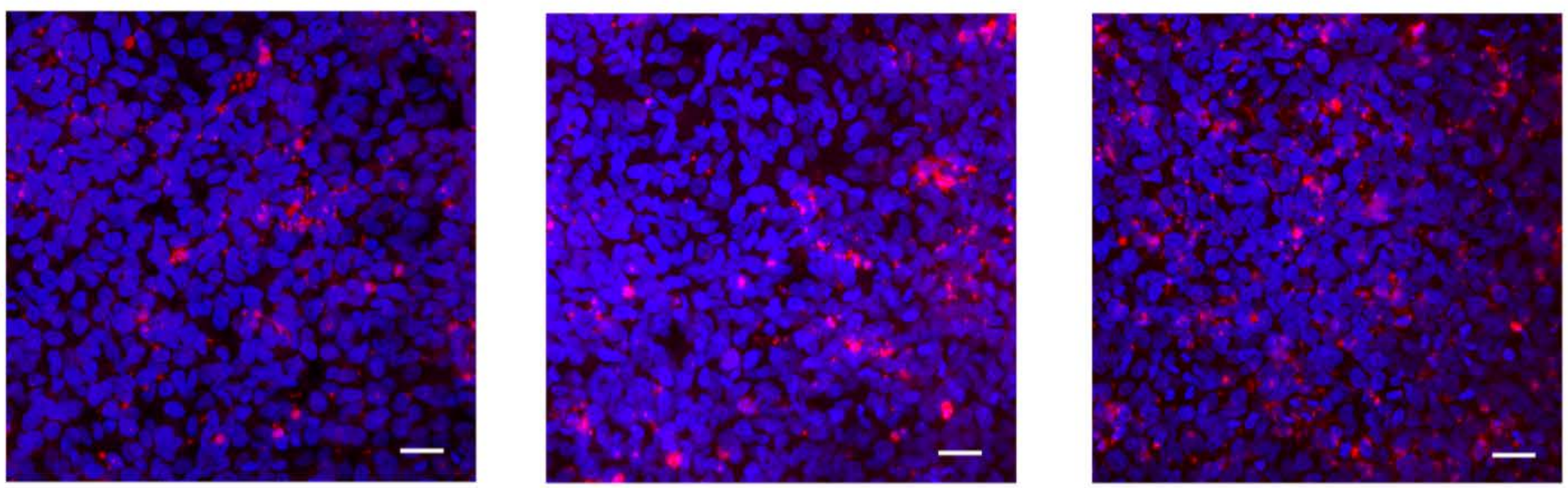

G

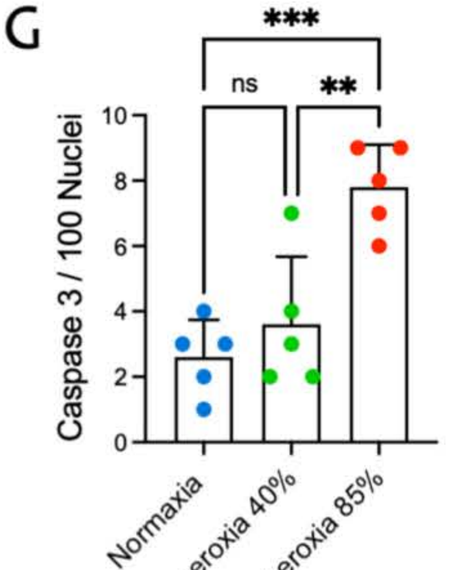

H

Z-projection

Coll IV DAPI

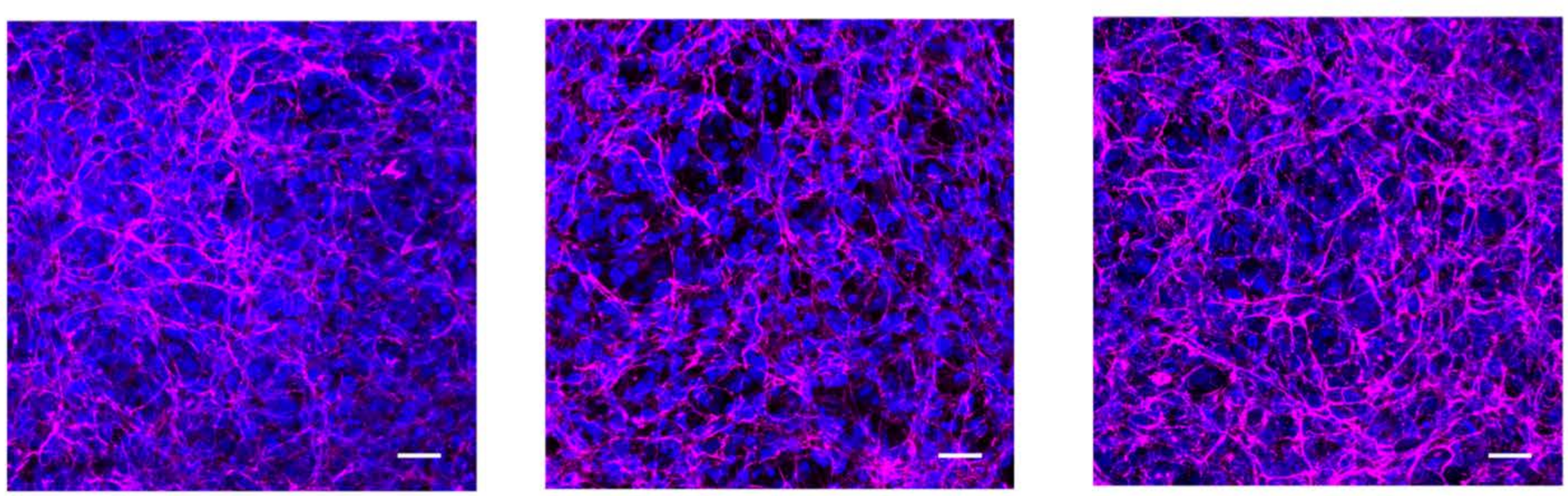

I

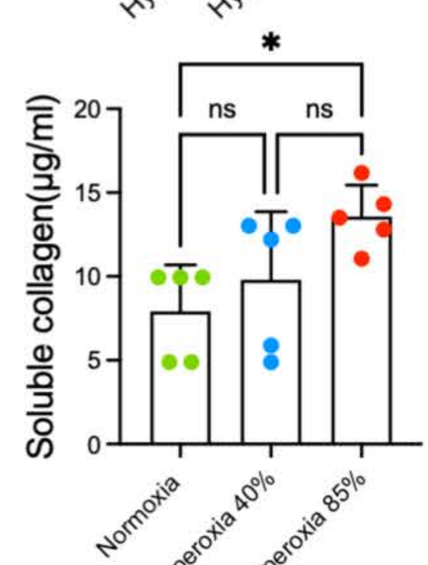

A

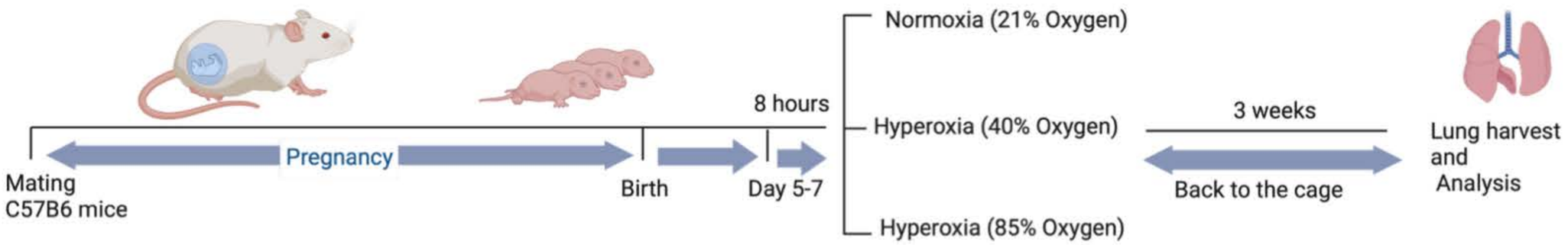

B

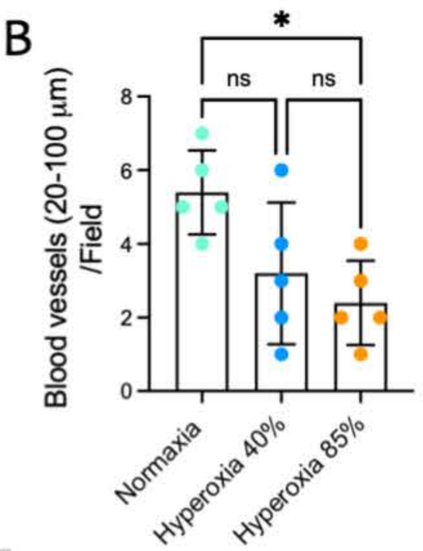

C

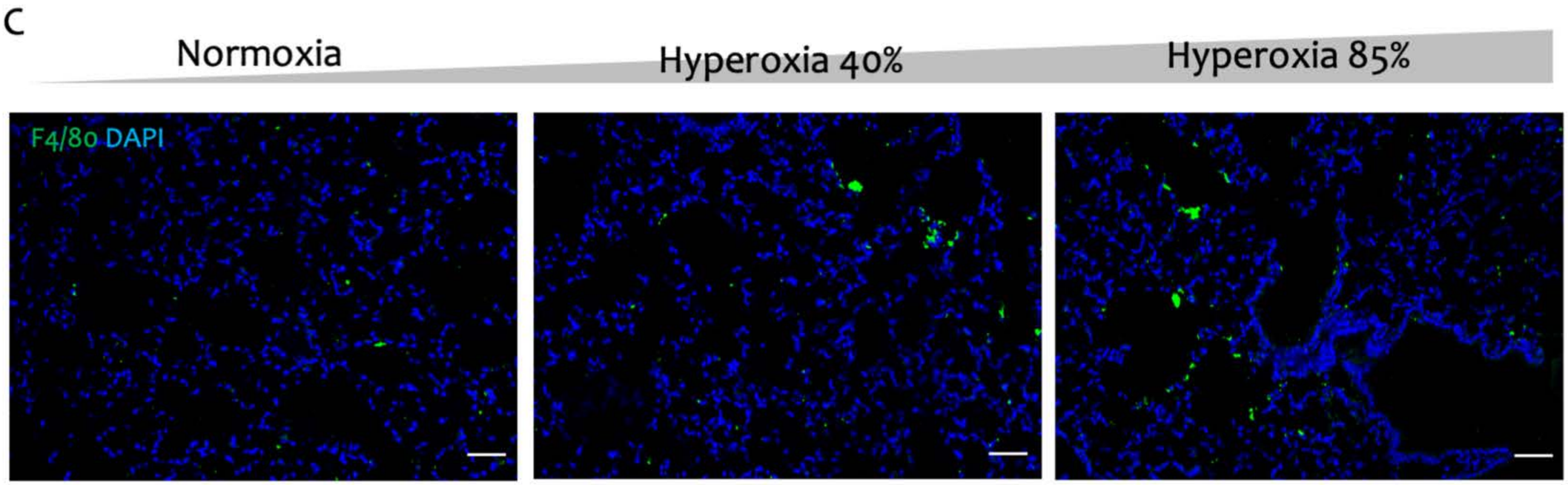

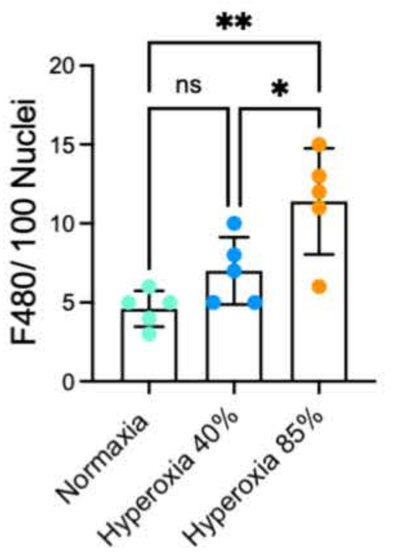

D

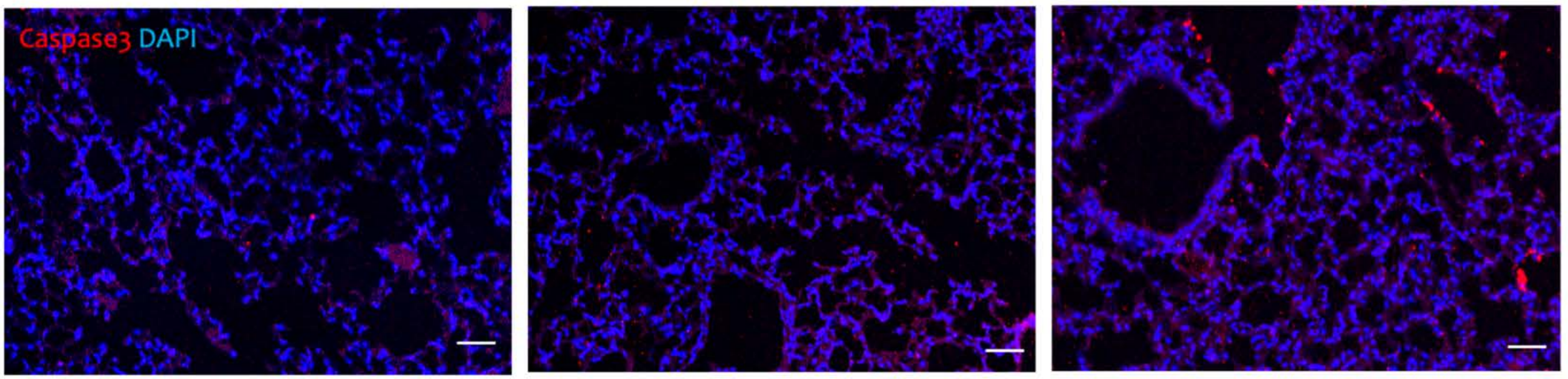

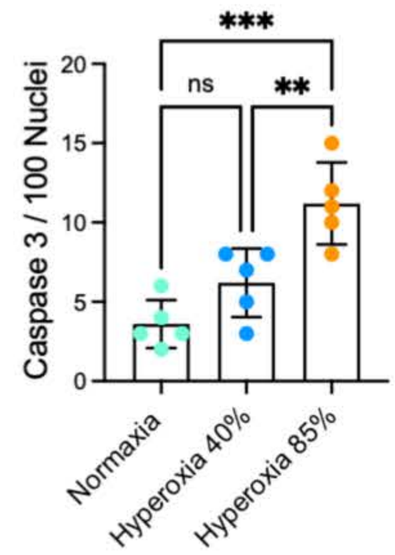

E

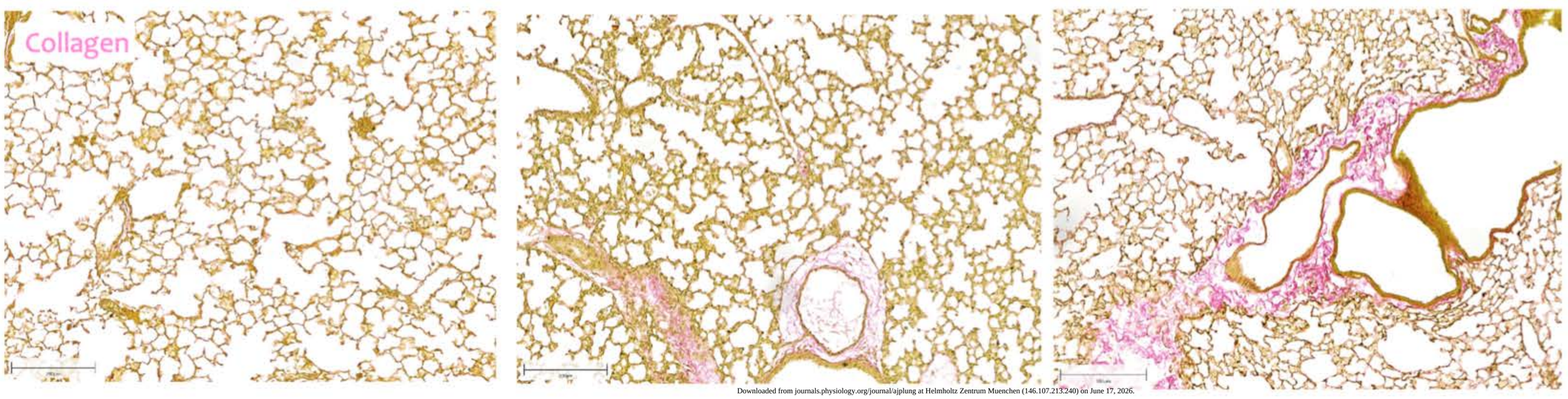

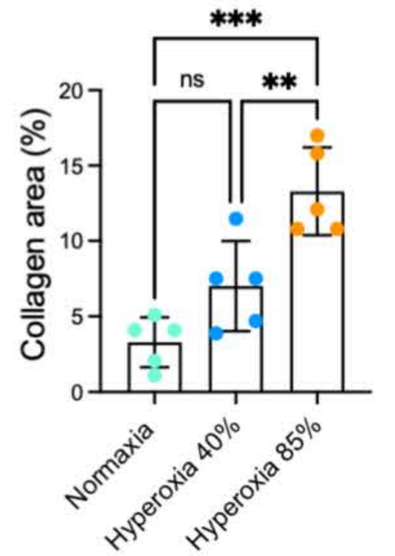

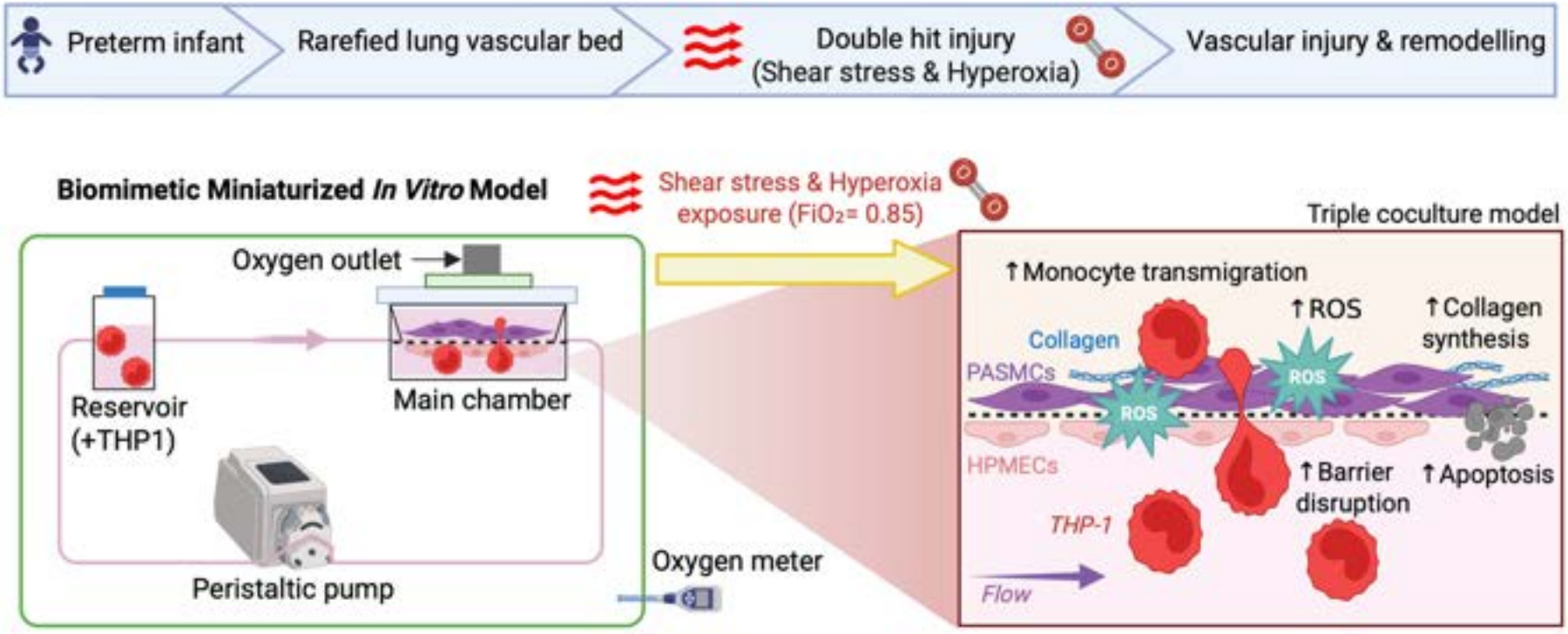

A biomimetic miniaturized *in-vitro* model that combines multiple-hit injury with a triple co-culture system provides an effective tool for identifying early neonatal pulmonary vascular injury